AFRL-OSR-VA-TR-2013-0140

Title, i.e, Synthetic Aperture Ladar for Tactical Imaging (SALTI)

David B. Allison,
University/Company

April 2013
Final Report

DISTRIBUTION A: Approved for public release.

AIR FORCE RESEARCH LABORATORY
AF OFFICE OF SCIENTIFIC RESEARCH (AFOSR)
ARLINGTON, VIRGINIA 22203
AIR FORCE MATERIEL COMMAND

REPORT DOCUMENTATION PAGE

Form Approved
OMB No. 0704-0188

Public reporting burden for this collection of information is estimated to average 1 hour per response, including the time for reviewing instructions, searching data sources, gathering and maintaining the data needed, and completing and reviewing the collection of information. Send comments regarding this burden estimate or any other aspect of this collection of information, including suggestions for reducing this burden to Washington Headquarters Service, Directorate for Information Operations and Reports, 1215 Jefferson Davis Highway, Suite 1204, Arlington, VA 22202-4302, and to the Office of Management and Budget, Paperwork Reduction Project (0704-0188) Washington, DC 20503.
PLEASE DO NOT RETURN YOUR FORM TO THE ABOVE ADDRESS.

1. REPORT DATE *(DD-MM-YYYY)*	2. REPORT TYPE	3. DATES COVERED *(From - To)*
12-5-2012	Final	30 Sept. 2009 - 30 Sept. 2012

4. TITLE AND SUBTITLE
Reconfigurable Nano-Plasmonics Holography

5a. CONTRACT NUMBER
FA9550-09-1-0698

5b. GRANT NUMBER

5c. PROGRAM ELEMENT NUMBER
AFOSR/NE

6. AUTHOR(S)
Blumberg, Girsh, Dennis, Brian S. and Haftel, Michael

5d. PROJECT NUMBER

5e. TASK NUMBER

5f. WORK UNIT NUMBER

7. PERFORMING ORGANIZATION NAME(S) AND ADDRESS(ES)
Rutgers, The State University of New Jersey, Piscataway, NJ 08854

Subcontractor:
University of Colorado at Colorado Springs, Colorado, CO 80918

8. PERFORMING ORGANIZATION REPORT NUMBER

9. SPONSORING/MONITORING AGENCY NAME(S) AND ADDRESS(ES)
Air Force Office of Scientific Research
Suite 325, Room 3112
875 Randolph Street
Arlington, VA 22203-1768

10. SPONSOR/MONITOR'S ACRONYM(S)

11. SPONSORING/MONITORING AGENCY REPORT NUMBER
AFRL-OSR-VA-TR-2013-0140

12. DISTRIBUTION AVAILABILITY STATEMENT
DISTRIBUTION A: APPROVED FOR PUBLIC RELEASE

13. SUPPLEMENTARY NOTES

14. ABSTRACT
We report experimental, theoretical and simulation results on the development of plasmonic holography by Reconfigurable Surface Plasmon Phase Modulators from micro-electromechanical devices. High dielectric constant nanostructures brought into the vicinity of propagating surface plasmon polaritons (SPP) will retard the SPP phase. SPP wavefronts could be manipulated in controllable and reconfigurable ways if multiple nanostructures are used to modify the phase. Prototypes were designed and fabricated with bi-layer Au doubly clamped free floating nanostructures that were lithographically ion milled, released and electrostatically actuated. We have experimentally demonstrated: 1) plasmonic slot waveguide coupling including propagation through SiO beam supports and under actuated beams; 2) SP focusing by a two dimensional SiO2 lens; 3) electrical gold beam actuation at 1 MHz; 4) diffractive changes in out-coupled light when beams are actuated and 5) enhanced SP coupling by Fabry-Perot resonators. Theoretical and simulation work has guided the experiments and device design resulting in: 1) efficient production of SPs from gratings; 2) understanding changes in phase and losses from SP waveguides characterized by SP propagation between Au films; 3) enhancement of SP intensity by Fabry-Perot resonators ; 4) maximizing SP propagation in the presence of transverse and longitudinal slits and 5) integration of the above components in a SP modulator device.

15. SUBJECT TERMS
surface plasmon, nano-photonics, phase modulation, reconfigurable

INSTRUCTIONS FOR COMPLETING SF 298

16. SECURITY CLASSIFICATION OF:			17. LIMITATION OF ABSTRACT	18. NUMBER OF PAGES	19a. NAME OF RESPONSIBLE PERSON
			SAR		Blumberg, Girsh
a. REPORT U	b. ABSTRACT U	c. THIS PAGE U			19b. TELEPONE NUMBER (*Include area code)* 732-445-5500 x2538

AFOSR Final Performance Report

Project Title: Reconfigurable Nano-Plasmonics Holography

Award Number: FA9550-09-1-0698

Start Date: Sept. 30, 2009

Program Manager:
Dr. Pomrenke, Gernot S.
Optoelectronics, THz and Nanotechnology
Directorate of Physics and Electronics
Air Force Office of Scientific Research
875 North Randolph Street
Suite 325, Room 3112
Arlington, Virginia 22203-1768 USA

Principal Investigator:
Prof. Blumberg, Girsh
Dept. of Physics and Astronomy
Rutgers, The State University of New Jersey
136 Frelinghuysen Rd.
Piscataway, NJ 08854
Phone: (732) 445-5500 x2538
Fax: (732) 445-4400

Co-Investigator:
Dennis, Brian
Dept. of Physics and Astronomy
Rutgers, The State University of New Jersey
136 Frelinghuysen Rd.
Piscataway, NJ 08854
Phone: (732) 445-5500 x2405
Fax: (732) 445-4400

Co-Investigator:
Dr. Haftel, Michael
Dept. of Physics
University of Colorado Colorado Springs
1420 Austin Bluffs Pkwy
Colorado Springs, CO 80918
Phone: (719) 255-3420

Table of Contents

Accomplishments

A. Introduction

B. Research, Device Development, Nanofabrication and Characterization

C. Facilities and Equipment

D. Simulation and Theory

E. Student Training

F. Conclusion

References

Accomplishments:

Investigators report progress made in the design, numerical simulation, process development, nanofabrication and demonstration of a prototype Surface Plasmon Modulator (SPM) micro-electromechanical system (MEMS) designed to manipulate and shape a surface plasmon polariton (SPP) wavefront. An SPM is composed of a double gold film plasmonic slot waveguide with an in-coupler grating, electrically actuated doubly clamped free floating gold nano-beams as the phase retarding modulators, an SPP focusing lens and an out-coupler slit.

a) Numerical Simulation, Design and Theory:

The main goals of the FDTD (finite difference time domain) simulations and theoretical aspects of our work in plasmonic holography was interpretation of results and to design devices that allow manipulation of the SPP phase across a wavefront, while at the same time enhancing the intensity and/or minimizing losses as the SPP wave propagates. Our simulations have explored several areas in this regard:

1) Efficient production of SPP waves from gratings.

2) Changes in phase and resulting losses from SPP waveguides characterized by having SPPs propagate between two gold films.

3) Propagation of SPPs in the presence of transverse and longitudinal slits (beams or electrodes) on either top or bottom of a plasmonic waveguide.

4) Focusing by an SPP lens.

5) Integration of beams, lenses and slits into an SPM device.

6) Enhancement of SPP intensity by using Fabry-Perot resonators.

b) Process Development and Nanofabrication of Protoype SPMs:

1) Deposition of a $Au/SiO_2/Au$ stack using TiO_2 as adhesion layer for Au to SiO_2.

2) Focused ion beam (FIB) lithographic patterning of free floating Au MEMS nano-beams, in-coupler gratings, plasmonic lens and out-coupler window/slits.

3) Use of liquid oxide etch to create free floating Au nano-beams.

4) Use of CO_2 critical drying to prevent Au nano-beams from sticking down after liquid etch.

5) FIB fabrication of plasmonic devices for SPPs decay measurement s after traversing longitudinal and transverse slits.

6) Fabrication of Au coated Si cantilevered pistons for phase interference measurements.

7) Potential conversion to parallel processing with e-beam lithography. Test structures were fabricated with 150 nm features.

c) Demonstration:

1) Simultaneous electrical actuation of six free floating Au beams at 1 MHz with stroboscopic interferometric profilometry (movie at http://girsh.rutgers.edu/MEMS/1MHz.avi).

2) Light coupling into a Au SPP slot waveguide via grating coupling.

3) SPP propagation through the plasmonic slot waveguide, including reflection and transmission through SiO_2 beam supports and lens.

4) Detection of focused out-coupled light by a two dimensional dielectric SPP lens.

5) Detection of diffractive changes in out-coupled light with SPP modulator beam motion.

6) SPP decay measurements after traversing longitudinal and transverse slits.

7) Enhanced plasmonic light coupling with a nano-structured Fabry-Perot resonator [1].

A. Introduction

This report describes the development, fabrication and characterization of prototype reconfigurable integrated electro-mechanical/nano-plasmonic devices that were designed to improve our understanding of the fundamental limitations in optoelectronics applications.

The problem that was addressed. Electronic integrated circuits are currently routinely manufactured with dimensions below 100 nm. Increased gate delays and excessive power density threaten the performance gains historically achievable by scaling integrated circuits. It is expected that beyond the 45 nm scale conventional copper interconnects will no longer support increased clock speeds and the industry will enter a new regime of electronic interconnect delay-limited performance. Optical interconnects could support increased data transmission rates of more than a thousand times that of current electronic interconnects, provided they could be integrated on-chip, controlled in two dimensions, and fabricated at sizes significantly smaller than the optical diffraction limit [2–9].

Surface plasmon polaritons (SPP) are electromagnetic waves that propagate at the interfaces between a metal and a dielectric by the collective motion of electrons in metal [10]. The electric fields associated with SPP modes are evanescent [11–13]. Being localized to the interface, SPP modes can be guided by subwavelength structures, which can form components for optoelectronic circuits. Such plasmonic circuits can consist of various elements such as plasmonic waveguides, switches, modulators [14–16], and couplers, which can be used to carry the optical signals to different parts of the circuit [9]. The SPP excitations can travel relatively long distances along metal interfaces thereby enabling novel ultra-fast optical and opto-electronic components and networks.

Recent works on light beaming in sub-wavelength periodically structured metal films suggest a direction for fabricating optical devices that utilize coherent SPP fluctuations and operate below the diffraction limit of propagating light [3]. *Significant advances in this area may be possible if SPPs can be controllably converted to and from free-space photons, and if their surface propagation can be intentionally reconfigured in two dimensions.*

Much previous work has been done in passive surface plasmon based optics [17–19] but the integration described above may be possible using reconfigurable surface plasmon-based optics, in which signals are transmitted by collective electronic oscillations confined to metal-dielectric interfaces that can be focused laterally to dimensions substantially smaller than light wavelength at comparable frequencies [3,10,19,20]. Successful integration of plasmonics with silicon technology radically depends on new intermediate coupling and control technologies such as development of a surface plasmon modulator [4–8, 15], nonlinear plasmonic devices [14, 21], waveguide components including interferometers, ring resonators [22], lenses [20, 23, 24], plasmonic waveguides as a means to confine and manipulate photonic signals, efficient coupling [1, 25] and others.

To this end the PI proposed development and fabrication of a prototype *Surface Plasmon Modulator* (SPM) device which can control the propagation of plasmonic signals with sub-wavelength spatial resolution and which can be reconfigured on the micro-second time scale. This modulation is possible due to the dispersion relation for surface plasmons which is defined by

$$k = \frac{\omega}{c}\sqrt{\frac{\epsilon_m(\omega)\epsilon_d}{\epsilon_m(\omega)+\epsilon_d}} \tag{1}$$

where $\epsilon_m(\omega)$ and ϵ_d are the frequency dependent dielectric constants of the metal and the dielectrics. For metal-air interfaces the SPP group velocity is just slightly slower than for free propagating light and therefore SPPs allow information transfer at significantly higher frequencies than today's electronic microprocessors. For the resonant frequency described by the condition $\epsilon_m(\omega) = -\epsilon_d$

the SPP wave-vector is the largest (Eq. 1) and phase velocity, $v = \omega/k$, the slowest. Therefore the phase velocity of a propagating SPP wave can be significantly reduced by the introduction of a highly dielectric material into the vicinity of the metallic surface and therefore the phase of a propagating plasmonic wave can be continuously controlled by local control of the effective dielectric constant. The proposed device would contain a linear array of metallic MEMS (micro-electro-mechanical system) actuators capable of sub-micron movement into and out of the field of a propagating SPP in a two dimensional (2D) waveguide.

When an actuator is attracted into the waveguide it will retard the SPP phase velocity in a small region or "pixel" near the actuator's center. If the pixel widths are smaller than the transverse dimension of the SPP mode then the small transverse pixel size should allow the phase front of the mode to be tailored to produce a desired propagation front. Therefore, a 2D holographic SPP intensity field is formed by interference of the phase modulated wave fronts of the incoming SPP mode.

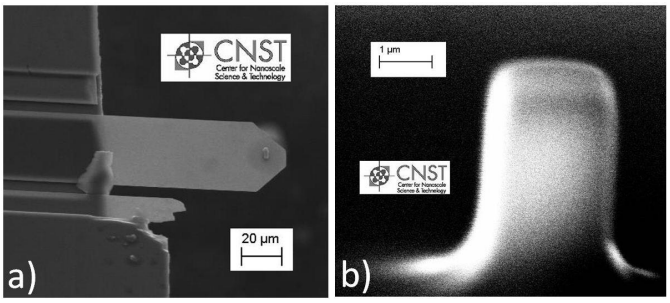

Figure 1: a) SEM of custom Au coated Si cantilever with piston. b) High magnification close up of piston.

Spatially compact reconfigurable plasmonic optics can be envisioned as the basis of very dense systems for optical signal processing [9, 14, 15, 26], high-speed intra-chip communications [4–8], and many other applications. The SPM device discussed here is an opto-mechanical interference device that provides local space-dependent control of phase retardation at any point of a coherent surface plasmon polariton wave front and, therefore, can control both the amplitude and phase of transmitted surface plasmon waves. Basic applications include fast and flexible switching, splitting, and focusing of plasmonic wave fronts, and, more generally, production of complex, rapidly reconfigurable propagating two dimensional electromagnetic fields. This technology can become the basis for a variety of reconfigurable systems, for example: 1) ultra-fast intra-chip communication can be performed by dynamically controlled propagating plasmonic waves [4–7, 15]; 2) the fast reconfigurable 2D pattern of modulated high-intensity electromagnetic fields enables fast multiplexing of a large array of phototransistors or field-effect transistors [26] and can be used as the basis technology for ultra-fast opto-electronic processors; 3) by employing non-linear effects in strongly enhanced electromagnetic fields the concept of an all-plasmonic transistor can be demonstrated [14], thus providing a critical component for direct signal processing in the optical domain as well as for more general optical computing technology; 4) plasmonic holography can be used as the basis for ultra-high resolution imaging, spectroscopic microscopy, and addressable high sensitivity spectroscopy [11–13].

Statement of work included: 1) design and nano-fabrication of a prototype device; 2) optical characterization and electrical calibration; and 3) demonstration of basic functionality of a prototype device. These steps will be described in detail in section B.

B. Research, Device Development, Nanofabrication and Characterization

B.1 Surface Plasmon Modulator elements: fabrication and demonstration.

Previous plasmonic device research of the PI and other researchers utilized fixed structures lithographically fabricated by focused ion beam (FIB) or e-beam lithography (EBL) and therefore,

did not provide adjustability of the plasmon optics. This can be seen in a number of plasmonic review articles [2, 27–29]. The need for dynamic adjustability is what drove the investigators to begin development of prototype free beam plasmonic MEMS devices to achieve the goals set out in the Section A.

B.1.0 Piston Cantilever Interferometer: The initial goal was to demonstrate proof of concept and show phase interference between SPPs on the air/Au and Au/glass interfaces of a single Au layer device with only in- and out-couplers. A custom gold coated Si piston at the end of a cantilever (Fig. 1) was fabricated and positioned between the SPP in- and out-couplers. The gap between piston and Au layer was controlled with AFM electronics and a piezo positioner (Fig. 2). Laser interference with the cantilever/piston masked demonstration of SPP interference and led investigators to change to the double clamped free beam MEMS device described next.

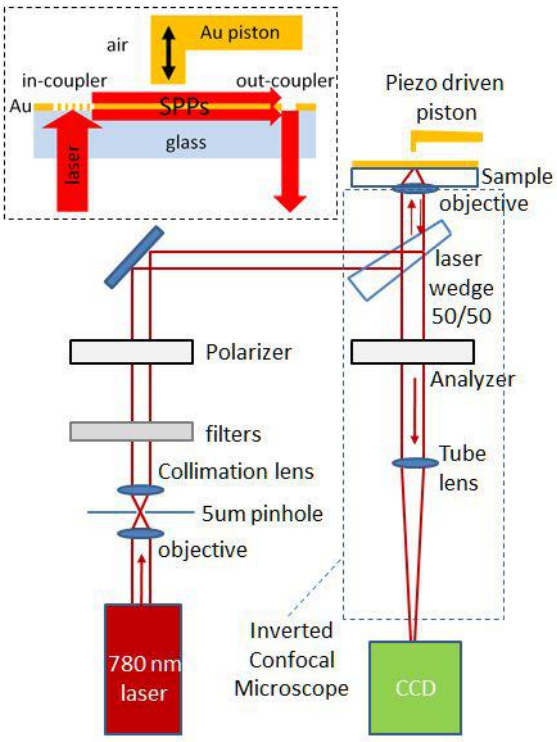

Figure 2: Schematic of plasmonic interferometer. Laser excitation and light collection from underneath sample using a 50/50 laser wedge. Inset (upper left) shows blow up of sample. Retardation piston slows SPP at air/Au interface and interference occurs upon recombination with glass/Au SPP at out-coupler slit.

B.1.1 Surface plasmon modulator description: The basic surface plasmon modulator (SPM) is a metal/insulator/metal stack with five main components: 1) MEMS beams cut into the top layer with the insulator removed underneath allowing free flotation; 2) an in-coupler grating on one side of the beams, also in the top layer and also with the insulator removed beneath; 3) an out-coupler slit on the other side of the beams in the bottom layer with the insulator and metal removed above; 4) a lens to focus SPPs onto the out-coupler slit and 5) electrodes for independent actuation of beams. Laser light from above coupled into SPP slot waveguide modes at the in-coupler grating, propagated through the waveguide, interacted with the beams and converted back to light at the out-coupler slit. The beams were electrically attracted to the bottom layer which allowed control of the waveguide gap. This locally changed the effective dielectric constant and phase retarded the SPP. If the beams are narrow and independently controlled then the SPP wave front could be arbitrarily manipulated (Fig. 3).

B.1.2 Phase retardation simulation: Before device fabrication PI verified that adequate SPP phase retardation is possible by attracting a free floating Au beam into a plasmonic slot waveguide. To estimate the effect, FDTD simulations were performed on the system shown in Fig. 4 similar to the SPM (see section D). Here an SPP on a single Au/air interface traversed through a Au/air/Au waveguide and emerged back to a single interface. The waveguide was formed by two 200 nm thick Au films separated by 250 nm of air and was 20 μm long. The top film was sliced into alternating beams with beams either attracted down by 100 nm or not. Plotted in Fig. 4 is the

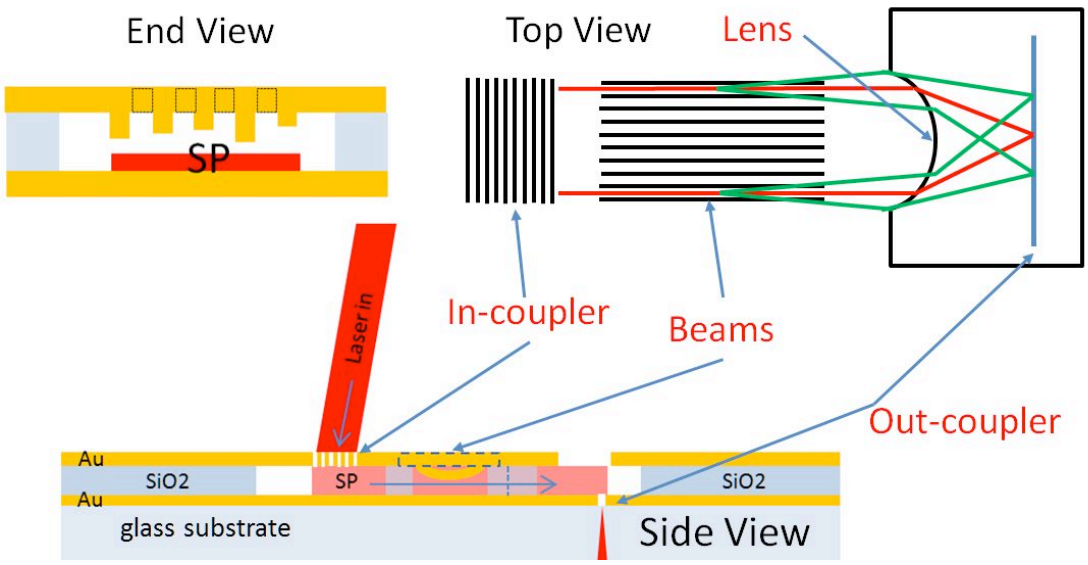

Figure 3: Schematic of Surface Plasmon Modulator device. Side View shows SPP in- and out-coupling with the SPP wave front confined in the plasmonic waveguide. The SPP intersects a linear array of free beam MEMS actuators capable of sub-micron controllable movement and introduce local and rapidly reconfigurable phase retardation in the SPP wave front. End View shows every other beam electrostatically pulled down to form a grating. Top View shows 0th (red) and $\pm$1st (green) order SPP diffracted by beams and focused by lens. Beam length is in tens of microns.

phase difference between an SPP from a down beam and an SPP from an up beam as a function of the length along the beams. As can be seen there is a phase difference greater than 3π which is more than required to perform SPP wave front manipulation.

B.1.3 Free floating Au beam MEMS.

B.1.3.1 Nanofabrication: The investigators first set out to establish that free floating Au beams could be achieved and actuated. To this end MEMS devices with doubly clamped free floating Au beams were designed and fabricated to demonstrate electrical actuation only (no in/out couplers or lens). They were fabricated lithographically with focused ion beam from a metal/insulator/metal stack, specifically Au/SiO_2/Au. Fabrication took place in a cleanroom environment at the National Institute of Technology Center for Nanoscale Science and Technology (NIST CNST). Processing entailed sputtering of 250 nm Au onto a glass substrate (with Cr adhesion layer) and plasma enhanced chemical vapor deposition (PECVD) of 250 nm SiO_2 (TiO_2 adhesion layer both sides) followed by a sputtered top Au layer of 250 nm (the beam layer). A final thin layer of tungsten (5 nm) aided the FIB lithography resulting in cleaner cuts and absorption of any SPP modes on the top Au layer.

Note that TiO_2 is a poor adhesive of Au to glass (as opposed to Cr or Ti) but it has low SPP absorption (imaginary part of refractive index $k = 0$) compared with Cr ($k = 4.36$) or Ti ($k = 2.92$) and adheres better than plain SiO_2. Two devices with six nano-beams each (20 microns long, 1 micron or 3 microns wide with beam separation of 150 nm) were cut into the top Au layer with FIB. The beams were then released in liquid oxide etchant (BOE) to remove SiO_2 from underneath. To prevent the free floating nano-structures from sticking to the bottom Au, as can happen from liquid surface tension when going directly from liquid to air, the device was dried in a CO_2 critical point dryer.

B.1.3.2 Electrical characterization: After fabrication, devices were characterized with an electrical probe station. Electrical shorts can occur between the top and bottom Au due to pinholes in the SiO_2 layer, redeposition of Au from ion milled cuts or metallic bridges across cuts. investigators demonstrated that pinhole shorts can become non-problematic by cutting a trench around the device to isolate it from the rest of the wafer thus, minimizing the number of pinholes. Careful application of current and voltage across the top and bottom Au layers got rid of redeposition and bridge shorts.

B.1.3.3 Beam Actuation at 1 MHz: Demonstration of electrical beam actuation was performed using electrical probes connected to the top and bottom Au layers to drive all beams simultaneously with one voltage supply. An interferometric profilometer at NIST was used to calibrate the beam displacement of fabricated devices. The beam displacement vs. applied voltage curve for a device is shown in Fig. 5b where beams were pulled down by approximately 80 nm with 7.5 V. Note that snap down occurs when the beam is pulled down more than one third of the gap resulting in a shorted device. 1 MHz dynamic beam actuation was also demonstrated using the interferometric profilometer stroboscopically synced to a 1 MHz sinusoidal excitation voltage (Fig. 5a). In a truly reconfigurable SPM each beam would be controlled *independently*. This measurement demonstrated that *all* free floating Au beams could be simultaneously actuated on a micro-second time scale.

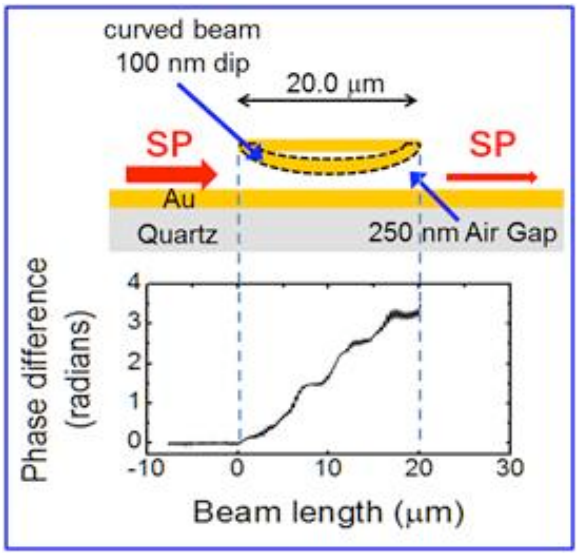

Figure 4: Graph: FDTD simulation of the phase difference between an SPP under a curved beam and an SPP under a straight beam as it traverses under the beams. Schematic: SPP on a single Au/air interface traverses through a Au/air/Au slot waveguide and emerges back to a single interface. The waveguide is formed by two Au films (200 nm) separated by air (250 nm). The top film is sliced into alternating beams with beams either curved down (100 nm dip) or straight.

B.1.4 Light coupling into a plasmonic slot waveguide: The investigators set out to demonstrate that light could be coupled into and out of the plasmonic slot waveguide between the Au layers in the free beam MEMS device just described. To accomplish this, new devices with beams, grating in-coupler, single slit out-coupler and SPP lens were fabricated (Fig. 6). Numerical analysis of SPP grating in-coupling was performed to determine the grating periodicity for optimal coupling into the waveguide for 780 nm laser excitation (see section D). Nanofabrication was similar to that in section B.1.3.1 except that an in-coupler grating and a lensed out-coupler window were cut into the top Au with FIB at the same time as the beams. After release no SiO_2 remained underneath the grating or beams and no SiO_2 was in the out-coupler region which served as a window to the bottom Au layer with the side closest to the beams in the shape of a lens (Fig. 3 Top). SiO_2 pillars between the beams and grating *and* between the beams and out-coupler window remained to support the free floating MEMS Au beams. Lastly an out-coupler slit was cut with FIB into the bottom Au layer at the calculated lens focal point.

Laser to SPP in- and out-coupling was demonstrated using an imaging inverted optical microscope customized with top laser focusing optics (Figs. 11 and 13). 780 nm laser excitation (from the top) coupled to slot SPP modes via the in-coupler grating into the Au/air/Au waveguide and propagated in a coherent collimated beam through the two air/SiO_2 interfaces of the first SiO_2

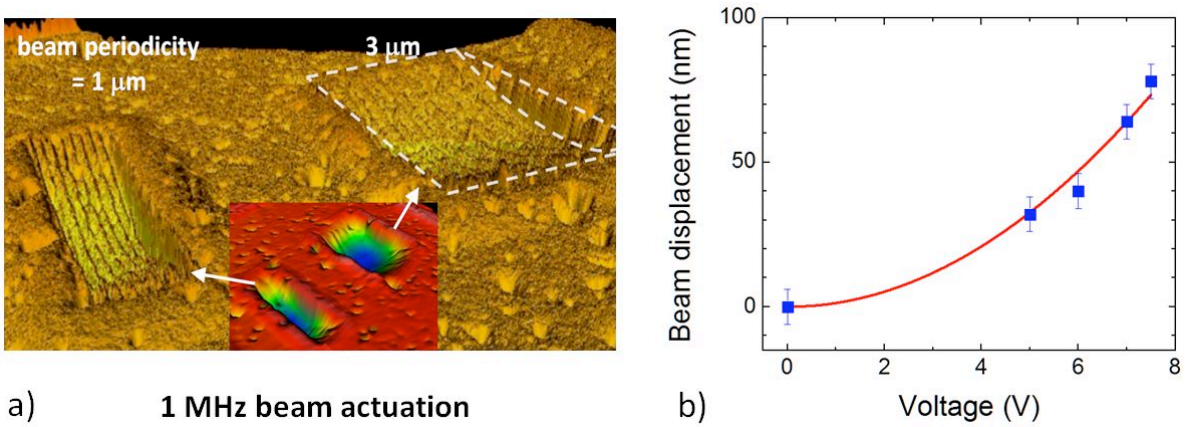

Figure 5: a) Interferometric snapshot of two prototype devices from a stroboscopic movie of 1 MHz electrical actuation of free floating MEMS gold beams. Beams are shown pulled down. Movie of 1 MHz sinusoidal actuation was made at 12 images/cycle and 4V peak to peak excitation. Inset is of same devices to clarify depth. White lines are guides for eye. Craters are interferometric artifacts. b) Beam displacement vs. voltage for an electrostatically attracted free floating MEMS Au beam. Beam length = 20 μm with a 250 nm air gap (Fig. 3). Red curve is a guide for the eye.

beam support. Propagation continued into the waveguide, composed of beams on top created from 150 nm wide longitudinal air slits in the gold film, and a continuous gold film below. The SPP next encountered the two dimensional SiO_2 lens which also acted as the second beam support. Propagation through the lens required penetration of two more air/SiO_2 interfaces onto the single air/Au interface of the out-coupler region. As shown in Fig. 6b a focused spot of light was detected at the out-coupler slit. The purpose of the lens and out-coupler window is discussed in sections B.1.5 where SPP diffraction is detailed.

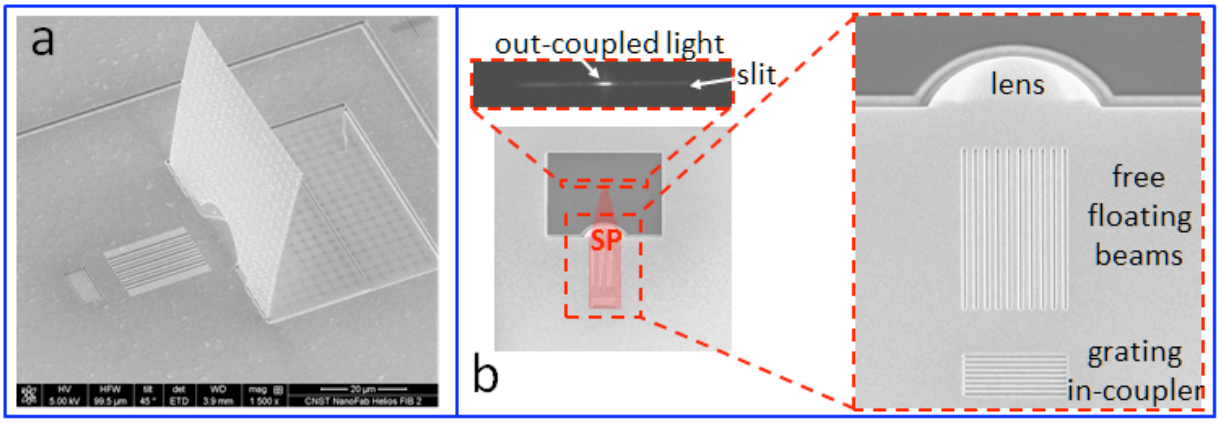

Figure 6: a. SEM image of a prototype MEMS device with free floating beams and lens. In-coupler grating is on the left, free floating double clamped Au beams are in the middle and out-coupling slit is on the right. A perforated flap can be seen that has been raised to almost vertical by micromanipulation to reduce stray laser light. b. SEM of device showing out-coupled light detected at the out-coupler slit. Laser excitation was from above with imaging from below. Blow ups show nanostructures (right) and optical image of out-coupler slit and focused light (top).

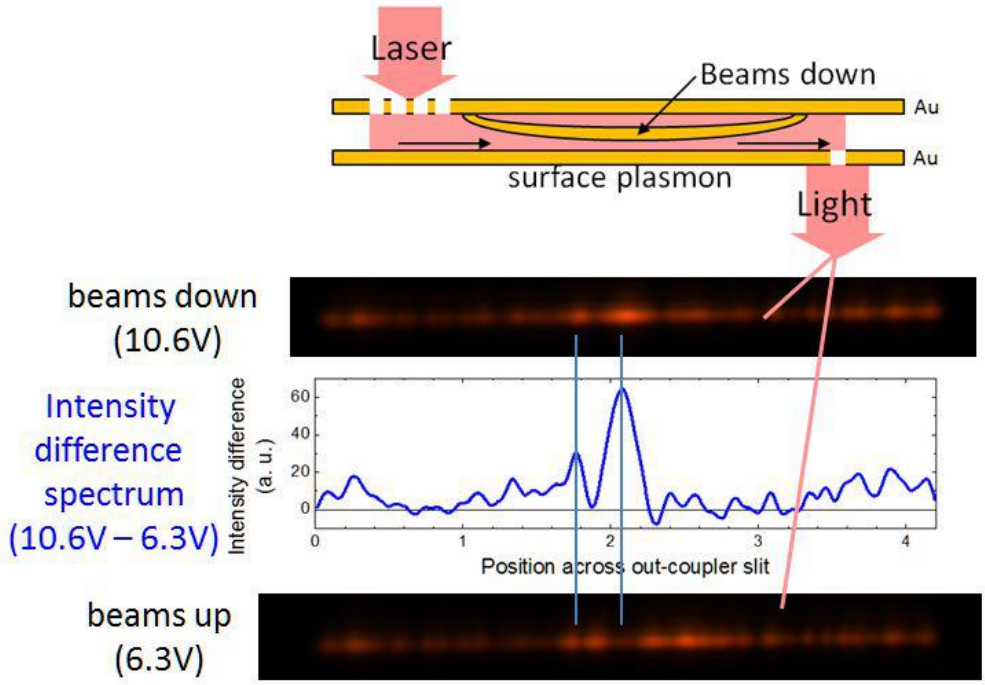

Figure 7: Top: Schematic showing plasmonic coupling with top laser illumination and bottom light collection. An SPM prototype with every other beam thinned was used to try to demonstrate diffraction from differential beam motion. Beams are shown electrically pulled down. Bottom: Optical images of out-coupled light with beams either up or pulled down. The plot is the intensity difference between the out-coupled light with beams down minus beams up. This is shown to demonstrate that diffractive changes in the out-coupled light were measured but due to beam nonuniformities the light pattern is complex.

B.1.5 Differential Beam Motion/SPP Diffraction: MEMS beam motion where all beams were actuated simultaneously was discussed in B.1.3.3. With *differential* beam motion (e.g. movement of every other beam) SPP diffraction could be demonstrated. This beam configuration, when actuated, would present a diffraction grating to the propagating SPP (Fig. 3 End View) and the lens would focus separated SPP orders onto the out-coupler slit. FDTD simulations were performed that predict adequate phase retardation occurs (Fig. 4) for SPP diffraction. A successful demonstration would show three focused spots of light at the out-coupler (0th and ±1st orders) when differential beam positioning is actuated and a single 0th order spot when not.

B.1.5.1 Beam Thinning for Differential Motion: Two different methods were tried to obtain differential beam motion. The first was thinning of every other beam by additional FIB ion milling (Fig. 6a). Interferometric profilometry showed that an applied electrostatic force pulled the thinner ion milled beams down more than unmilled beams. Although the investigators w not able to clearly show SPP diffraction orders, diffractive changes in the out-coupled light were seen when the out-coupled light was compared between beams up (un-actuated) and beams down (actuated) (Fig. 7). The complex nature of the out-coupled light is due to beam nonuniformity, stray laser light and thinned beams were not evenly attracted to the bottom Au layer. This technique was eventually abandoned because of beam nonuniformity and internal stresses that caused beam bowing (up and down) with time.

B.1.5.2 Actuation via Electrode Pads: The other method used to obtain differential beam motion required two separate lithographic FIB millings to create wires and electrode pads to beams, the second *after* the beams were written and released. Every other beam was connected together and to an electrode pad *or* each individual beam was connected to an independent electrode pad (Fig. 8). This technique had a different set of problems associated with it. Serious shorting between the top and bottom Au layers was measured and thought to come from redeposition of the secondary ion milled Au inside the waveguide. Also, the necessary overlapping of cuts from different FIB sessions, due to imperfect realignment, caused ion milling of the bottom Au layer. This allowed stray laser light to penetrate the bottom Au layer, interfering with the imaging of the weak out-coupled light from underneath. Beam nonuniformity was also seen from the secondary FIB cuts. This technique was also abandoned because of beam nonuniformities and stray light issues.

B.1.5.3 Individual Electrodes and PMMA Protective Layer: Investigators began new development of multi-electrode devices by lithographically writing all nano-structures (beams, wires, pads and couplers) in one FIB session. The release process is different with electrode wires involved since during release the wires connecting the beams to pads must be protected from the liquid oxide etchant or else there will be no support from underneath and the wires and beams will collapse and short. Protecting these structures with materials resistant to the oxide etch is

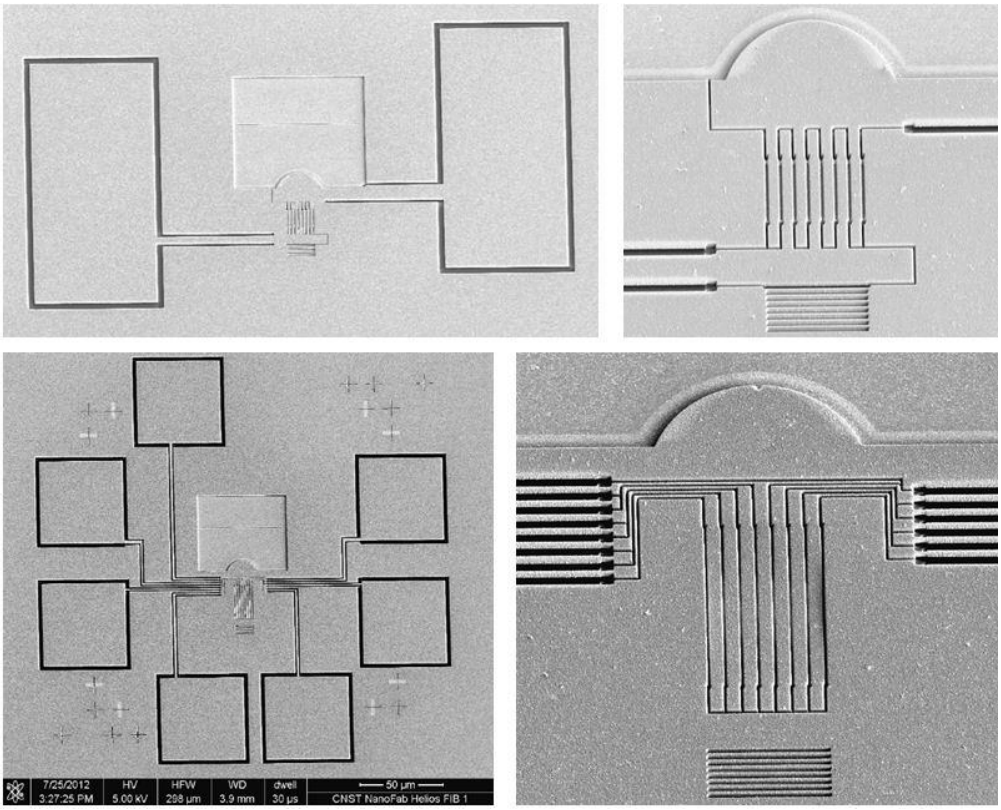

Figure 8: SEMs of multi-electrode SPM prototypes fabricated with two separate FIB sessions. Top: Every other beam is connected together and to an electrode pad (two pads). Close up shows realignment offset of beams to electrodes. Bottom: Every beam is connected to an individual electrode pad (seven pads). Close up shows beam on the right stuck down to bottom Au layer.

therefore necessary and was possible using PMMA (poly-methyl methacrylate), a common positive resist for e-beam lithography which is known to withstand liquid oxide etchant of low concentration. This was done by spinning on PMMA and then areas with structures that need to be released were exposed with EBL and developed away. When the device was etched, only the areas without resist were released. Fabrication after metal/insulator/metal deposition includes: 1) FIB of *all* beam structures; 2) Spin on PMMA and then EBL to open release windows; 3) Develop away exposed areas and release beams, etc., in liquid oxide etch; 4) remove PMMA by solvent; and 5) CO_2 critical point dry.

B.1.6 Wirebonding to electrode pads: With only two electrode pads it was reasonable to electrically actuate beams with electrical probes. With eight electrodes wire bonding interconnections from individual electrode pads to a multi-pin header is necessary to connect to a multi-output voltage source. Wire bonding is challenging since the top Au layer is poorly adhered to the bottom Au layer with TiO_2 (to prevent SPP absorption) and the top Au tears off as the wire bonder is retracted.

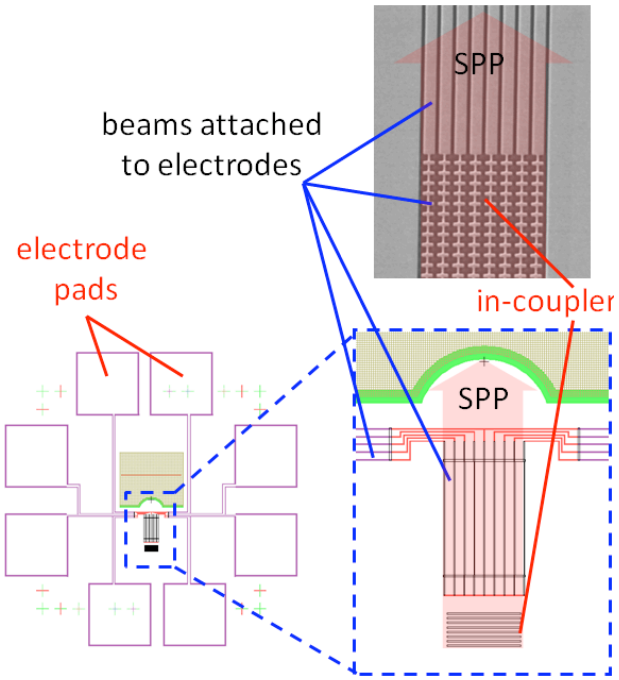

Figure 9: Bottom: Schematic of prototype 8 pad SPM. Blow up shows how the SPP propagates through electrode wires that connect to beams. Top: Corrugated electrode wires act as the grating in-coupler so the SPP will not have to traverse wires. These corrugated gratings were experimentally shown to produce SPPs.

The PI began to develop a process to work around this issue by wire bonding to the *bottom* Au layer where there is strong adhesion of Au to glass due to Cr adhesion. Electrode pads in the bottom Au were cut with FIB that were electrically isolated from the rest of the bottom layer. This took place *before* the middle SiO_2 and top Au layers were deposited. Then, during the FIB of the top Au layer, structures electrically connecting the bottom pads to the top beam wires were cut above the bottom pads so that after the oxide release an electrical connection was made by dropping down to the bottom pad since there was no support underneath.

The connection of wires to beams can take place either in the SPP beam path or by making the grating in-coupler from corrugated wires (see Fig. 9 right: top and bottom). The feasibility of both electrode configurations was shown in both FDTD simulations of SPP propagation over narrow longitudinal and transverse slits (see section D) and experimentally from out-coupled light in devices fabricated with in-couplers made of corrugated wires.

B.1.7 Conversion to EBL processing. If demonstration of reconfigurable wave front manipulation had been achieved the investigators intended to optimize SPMs by varying device parameters. The initial use of FIB is appropriate for small numbers of devices to show basic functionality. Optimization is more appropriately done using EBL for fabrication since large numbers of devices can be processed in parallel and the wide variety of device variations is more easily achieved. To this end investigators worked in parallel with the Argonne National Laboratory

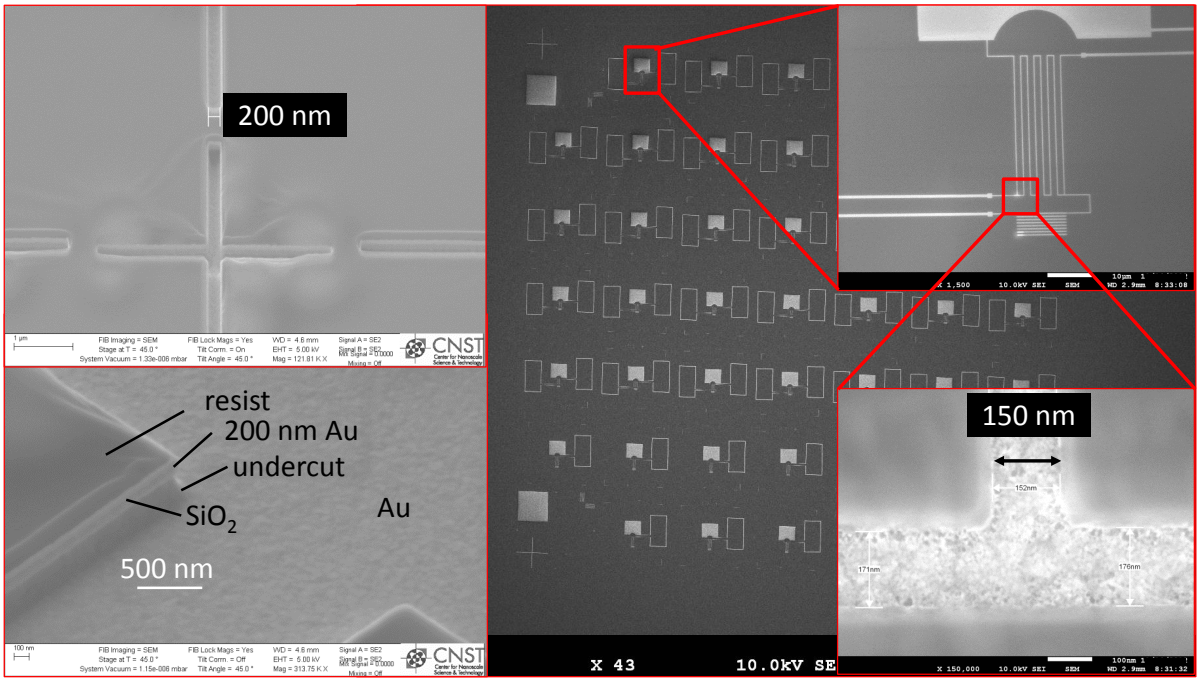

Figure 10: SEM images of test structures patterned with EBL at the Argonne CNM. Right: Parallel processing of SPM devices. Insets: 150 nm linewidths of EBL patterns after developing e-beam resist. Left: EBL test structures after ion milling at the NIST CNST. Clean 200 nm wide cuts with straight sidewalls were achieved (top) with slight undercutting of SiO_2 (bottom).

Center for Nanoscale Materials (ANL CNM) where, in collaboration with Dr. D. Lopez, the investigators began development of an EBL process to make such devices. This required optimization of e-beam parameters such as beam current, trench depth vs. dose, resist type and thickness, etc. There were promising preliminary results using test structures written with EBL at ANL CNM that were subsequently ion milled at NIST (Fig.10). Here the ion miller made use of a broad Ar ion beam rather than a focused Ga ion beam (FIB) to controllably and uniformly process devices in parallel. The ion miller operating parameters also required optimization.

B.1.8 Status of SPM development at end of funding period.

B.1.8.1 Simulation: The experimental results and current design were guided by investigator's theoretical and FDTD simulation studies of: 1) efficient production of SPPs from the coupling gratings; 2) understanding changes in phase and losses from SPP waveguides characterized by SPP propagation between Au films (Figs. 4); 3) maximizing SPP propagation in the presence of transverse and longitudinal slits; and 4) integration of beams, lenses and slits in a SPP MEMS device. See section D for a complete discussion of all simulation results.

B.1.8.2 Fabrication and demonstration: Investigators have made progress in the design, process development and fabrication of doubly clamped free floating Au beam MEMS. Typically MEMS do not use Au for mechanical motion and therefore developmental work has been required. Investigators have successfully fabricated prototype devices and experimentally demonstrated: 1) deposition of a $Au/SiO_2/Au$ stack using TiO_2 as adhesion layer for Au to SiO_2 without delamination upon exposure to air (since TiO_2 is a poor adhesive); 2) FIB patterning of device nano-structures;

3) use of liquid oxide etch to release beams without separation of Au from support structures (again, since TiO_2 is a poor adhesive); 4) simultaneous electrical actuation of six Au beams at 1 MHz, which gives credence to the stated goal of reconfigurability on the micro-second time scale (Figs. 5a - b); 5) light coupling into a Au SPP slot waveguide via grating coupling, SPP propagation through the waveguide (including reflection and transmission through SiO_2 beam supports) and detection of focused out-coupled light after a two dimensional dielectric lens (Fig. 6); 6) diffractive changes in out-coupled light with differential beam motion (Fig. 7) and. 7) 200 nm linewidth cuts from ion milled e-beam lithography test structures.

B.1.9 Enhanced coupling between light and surface plasmons by a nano-structured Fabry-Perot resonator. The investigators have demonstrated through experiment and simulation enhanced photon to SPP coupling using subwavelength metallic gratings and a variable gap Fabry-Perot (FP) resonator. Enhancements of out-coupled light intensity of 15x were measured when compared to systems with no resonator. Out-coupled intensities showed a FP type resonance when the resonator gap was scanned. Finite-element time and frequency domain simulations supported the measured results [1].

C. Facilities and Equipment

C.1. Facilities at PI's Rutgers laser lab.

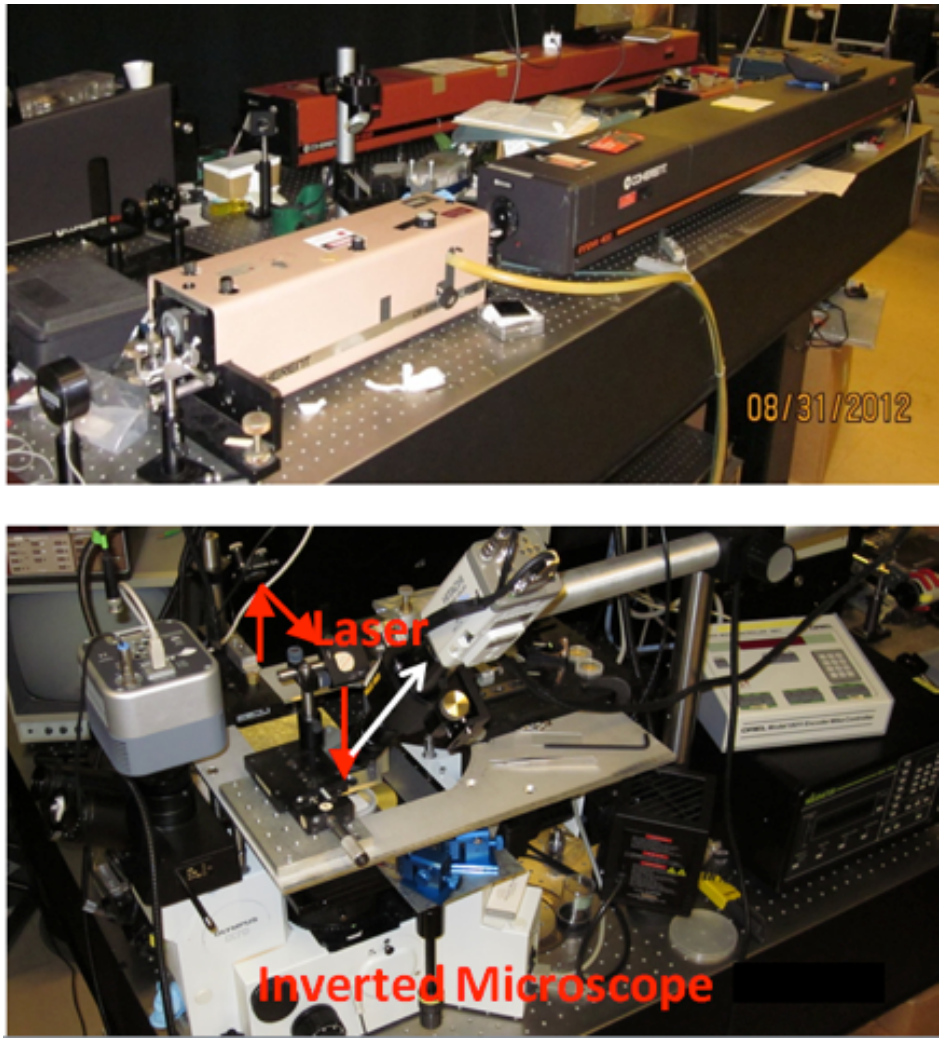

Figure 11: Optical equipment in Prof. Blumberg's lab at Rutgers. Top: tunable lasers include Kr ion pumped dye laser and Ar pumped Ti:Sapphire laser. Bottom: Inverted microscope set up with top laser illumination, top imaging, high sensitivity cooled CCD camera, electrical probes and wavemeter.

The PI's laser spectroscopy laboratory at Rutgers University is a world-class facility equipped with a custom-built aberration free fast triple stage Raman spectrometer with record-breaking sensitivity, resolution, and stray light rejection, a collection of pump (Kr+ and Ar+ Innova lasers, Coherent) and tunable lasers covering the spectral range between 0.33 and 1.5 micrometers (Ti:Sapphire/dye 899, Coherent, Tunable Diode Laser SDL TC40, and others), liquid helium temperature cryogenic equipment, 11 Tesla superconducting magnet, a high resolution near field scanning probe microscope (Nanonics), a collection of high-resolution confocal Raman microscopes (Leica and Olympus), sensitive imaging detectors, etc. This laboratory was developed by the PI and his collaborators at Bell Labs and was purchased by Rutgers University and moved to the PI's new lab at the Dept.of Physics and Astronomy on the Busch Campus in Piscataway, NJ.

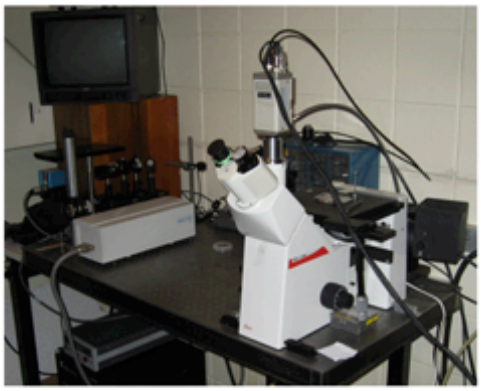

Laser optics table and custom inverted microscope

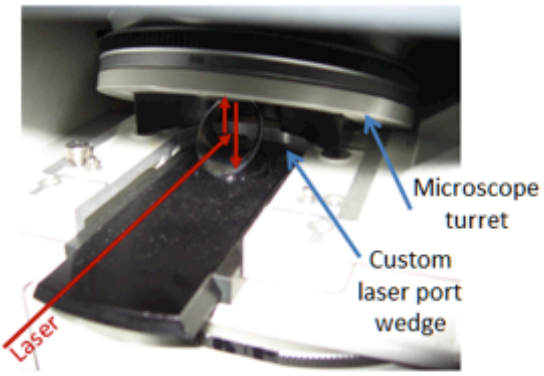

Custom inverted microscope laser beamsplitter

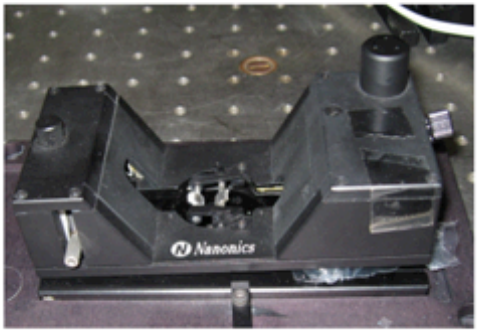

Piezo positioner for inverted microscope

Ultra low noise
piezo controller
and AFM electronics

Figure 12: Optical equipment in Prof. Blumberg's lab at Rutgers includes NSOM imaging system with Oxford electronics and Nanonics piezo head, custom inverted microscope with laser port and tunable solid state near infrared laser 780 nm.

C.2. Facilities at NIST Center for Nanoscale Science and Technology

The NIST Center for Nanoscale Science and Technology (CNST) supports the U.S. nanotechnology enterprise from discovery to production by providing industry, academia, NIST, and other government agencies with access to world-class nanoscale measurement and fabrication methods and technology. The CNST's shared-use NanoFab gives researchers economical access to and training on a state-of-the-art tool set required for cutting-edge nanotechnology development. PIs access to CNST Nanofab is under Facilities use agreement FU-10-014.

The Nano- optics/MEMS lab will be available to investigators through collaboration with Dr. V. Aksyuk on the project of MEMS controlled reconfigurable plasmonics holography based on large optomechanical coupling of plasmons in tunable slot waveguides.

Figure 13: Nanofab equipment used at NIST CNST.

C.3. Facilities at ANL Center for Nanoscale Materials

PIs access to CNM Nanofab is under Facilities use agreement CNM 27389.

The most relevant tools for Surface Plasmon Modulator development at CNM: Electron Beam Lithography System: JEOL 9300. Focused Ion Beam: FEI Nova 600 NanoLab. Deposition: Oxford Plasmalab 100 Inductively Coupled Plasma Enhanced Chemical, Vapor Deposition, Sputter deposition system (Emitech K675X).

Nanofabrication and Devices group leader: Dr. Daniel Lopez. The Nanofabrication and Devices Group is advancing the state of the art in nanofabrication and the fundamental science of nanoscale systems. Their research program involves a multidisciplinary approach combining theory, simulation, and experiments to understand the fundamental processes governing the fabrication and integration of nanoscale materials and devices, and by this means, to work toward the design of functional nanoscale systems and novel phenomena. The group is creating new processes capable of achieving sub-10-nm critical dimensions with large area patterning. Micro- and

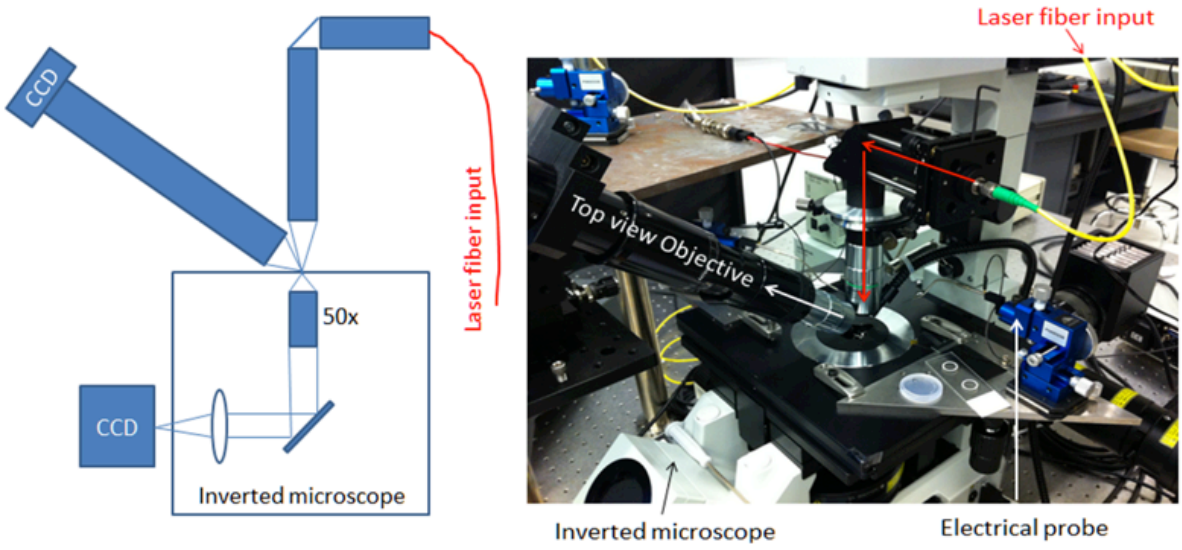

Figure 14: Experimental optical set up of the SPM imager in the NIST Optical MEMS lab of Dr. V. Aksyuk. Left: Side view schematic of experimental set up. 780 nm fiber laser is input from top and focused onto SPP grating in-coupler with 20x objective. Bottom 50x objective images out-coupled light. Top imaging 10x objective at 45 deg is used for electrical probe placement and laser alignment. Right: Photograph of inverted microscope with top imaging and focusing optics and electrical probes.

nano-electromechanical systems are being developed as platforms for manipulation and control of nanostructures and for microenergy harvesting.

D. Simulation and Theory for Plasmonic Holography

D.1 Background

There are three main purposes in the simulation and theoretical aspects of our work in plasmonic holography. They are (1) to guide the experiments and design of devices; (2) to explain experimental results; and (3) to explore the design parameter space that may be outside that explored experimentally. The main goal is to design devices that allow manipulation of the surface plasmon polariton (SPP) phase across a "wavefront", while at the same time enhancing the intensity and/or minimizing losses as the SPP wave propagates. Our simulations, using the High Accuracy Scattering and Propagation (HASP) code have explored several areas in this regard: (1) The efficient production of SPP waves from gratings; (2) the changes in phase and resulting losses from SPP waveguides characterized by having SPs propagate between two metal (in our case gold) films; (3) enhancement of SPP intensity by using Fabry-Perot (FP) resonators ;(4) the propagation of SPs in the presence of transverse and longitudinal slits on either top or bottom of the SPP waveguide; (5) integration of the above components in a SPP modulator device. We describe the results of simulation and theory on these topics in the sections that follow.

Our main tool for the required EM simulations is the High-Accuracy-Scattering and Propagation (HASP) code [1,32]. The code was written at the Naval Research Laboratory by one of the co-investigators (MIH), and has been used extensively for investigating advanced photonic materials, especially those that exploit SPP processes [32-34]. The HASP code is a finite-difference-time-domain (FDTD) code that employs a finite difference algorithm that is similar to the widely used Yee algorithm [35], but is much more accurate while still being of first order. The simulations yield the EM fields as a function of the spatial coordinates and time. Frequency content is easily obtained either by FFT techniques (when the incident wave is a short pulse) or by running at a fixed frequency (i.e., the incident wave is highly monochromatic). The code also has specific features to handle the negative-complex dielectric constants that describe metals in the visible and IR regimes where surface plasmons can be supported. This program has been optimized for parallel computation by utilizing Message-Passing-Interface (MPI) programming that has increased the computational speed by an order of magnitude. Typical CPU (per processor) times are now less than 1.0 μsec per spatial point per time step per processor on highly parallelized platforms. Most computations were carried out on the HP 4700 at the Air Force Research Laboratory at Wright-Patterson AFB and on the SGI Altix Ice at the US Army Engineer Research and Development Center (ERDC) of the DOD Supercomputing Resource Center (DSRC) in Vicksburg, MS, under the DOD High-Performance Computation Modernization Project (HPCMP).

Simulations basically amount to "numerical experiments". It is always challenging to reproduce the experimental conditions in finite-difference simulations. Key difficulties are (1) truncation errors in amplitude and phase brought about by the finite gridding as well as resolution of features on the nanoscale from such gridding; (2) truncating an open system by a finite computational volume, i.e., boundary conditions. The HASP algorithm is a vast improvement over the more commonly used Yee algorithm with regards to truncation errors, but for the complicated nanostructures simulated we have found a grid spacing of ~.01 λ is necessary to get good resolution. This leads to very CPU and memory intensive computations. The multiple-processor capability of the computers in the DOD High Performance Computation Modernization Project has proven very helpful in this regard. With regard to boundary conditions the main problem is to minimize artificial reflection from the boundaries of the computational volume. These have been minimized by employing the Perfectly Matched Layer (PML) method [36] developed over the last 20 years, but still there is some difficulty applying this to a metal with its negative dielectric constant. To circumvent this difficultly we have always surrounded the

metallic regions with air, which introduces its own artificial reflection (a couple of percents). Thus some algorithmic development is needed here.

Finally, theoretical understanding is very helpful in interpreting experimental and simulation results. A promising approach appears in ref. [37] and related work [38]. This theory applies an electromagnetic (em) version of the tight binding (TB) formalism, used extensively in solid-state physics, to the problem of light, and in particular SPs, interacting with sub-wavelength slits and grooves. In this approach the fields inside of defects, such as holes, slits, and grooves, are expanded in terms of the fields produced by a perfect conductor (PC), except with an appropriate boundary condition for the real metal applied at the metal-dielectric interface. Details of this theory appear elsewhere [37,38], and one needs to bear in mind that this theory is most valid when the defects are much smaller than a wavelength. We include theoretical analyses using this approach when applicable, i.e., when there are interactions between slits or grooves with SPs.

D.2 Launching Surface Plasmons

Almost any defect on a metal surface can launch SPP's, but to maximize the intensity for a particular frequency requires a regular periodicity of such defects matched to the SPP wavelength. In this report we determine the SPP intensity when SPP's are launched by an array of holes, by a grating of slits, and by a single slit. Here one has to trade off the experimental simplicity of employing a single slit with the larger intensities obtainable from the periodic structures that are more complicated to handle experimentally.

It is a well-known result from the physics of plasmons that Maxwell's equations supports surface plasmons9 , i.e., EM fields propagating along but localized near metal surfaces (or metal-dielectric interfaces) (from above and below), where the SPP propagation wave number k_{sp} along the surface is given by

$$k_{sp} = (\omega/c)(\varepsilon_d\, \varepsilon_m /(\varepsilon_d + \varepsilon_m))^{1/2}, \qquad (1)$$

where ω is the angular frequency, c the velocity of light, ε_d the dielectric constant of the dielectric (or vacuum), and ε_m the dielectric constant of the metal. A defect (hole, slit, impurity, etc.) on a metal surface, through interacting with the incident radiation, can launch an SPP as long as the condition

$$\boldsymbol{k}_{inc,s} + \boldsymbol{k}_{d,s} = \boldsymbol{k}_{sp}, \qquad (2)$$

is satisfied, where $\boldsymbol{k}_{inc,s}$ is the surface component of the wave number (or photon momentum) of the incident EM field, and $\boldsymbol{k}_{d,s}$ is the wave number (or momentum) transferred to the incident photon by the defect or defects interacting with the photon. Defects on the surface will normally produce a distribution of $\boldsymbol{k}_{d,s}$, related to the Fourier transform of the defect profile, and the efficiency of coupling to SPP's will be determined by that part of the distribution that satisfies Eq. (2). The most efficient coupling occurs when the defects are uniform and form a regular periodic structure, in which case the $\boldsymbol{k}_{d,s}$ distribution is sharply peaked about

$$\boldsymbol{k}_{d,s} = 2\, n\pi / a_x\, \mathbf{i} + 2\, m\pi / a_y\, \mathbf{j}, \qquad (3)$$

where n and m are positive or negative integers, and a_x and a_y are the periodic lengths in the x and y directions, respectively. Eqs. (1) - (3) infer that one can control the frequency and direction of SPP propagation by the direction and frequency of incident radiation and by having a lattice of defects with a specified periodicity. The SPP resonance will have a finite width because (1) the dielectric constant of real metals has a small but finite imaginary part in the visible and IR, and (2) the defects, even if perfectly periodic, are not perfect sinusoidals and do not yield delta function $\boldsymbol{k}_{d,s}$ distributions. Furthermore, any departure from pure periodicity will further introduce a finite width to the $\boldsymbol{k}_{d,s}$ distribution. In general Eq. (3) is more of a guide than an exact equation, and to really determine how efficiently certain defects launch SPs requires more accurate theoretical or numerical analysis.

We found out rather quickly that simulations for SPP generation indicated that periodic slit gratings were much more efficient than arrays of holes. The reasons for this are: (1) more em radiation is incident on a slit of length a then on a corresponding square hole of area a^2; (2) all the SPP modes produced by slits are directed perpendicular to the slit, whereas holes yield modes in many different directions (see Eq. (3)). In light of this we concentrated our attention on the roles of the input slit widths and periodicity in launching SPs. In optimizing the grating spacing and width of the slits we found that the SPP intensity can vary by a factor of ten or more even with relatively small changes in either parameter.

Our simulation setup was similar to our original experimental setup: a 200 nm gold (Au) film is atop a glass substrate irradiated by a 780 nm laser from below (i.e., through the glass substrate) at normal incidence. (Fig. 17 in the next sections gives an illustration of this). SPs are launched from the input slits, of width w and periodicity d that go entirely through the Au film. We consider the cases of 4 such input slits and also just a single slit. Surface plasmons will appear on both interfaces of the Au film, but with different wavelengths according to the relation of Eq. (1) ($\varepsilon_d = 1.0$ for Au-air interface, $\varepsilon_d = 2.35$ for Au-glass interface). In the near IR $|\varepsilon_m| >> |\varepsilon_d|$ and, by Eq. (1) the SPP wave length is close to the wavelength in the dielectric medium (or vacuum), and hence by Eqs. (2)-(3), for normal incidence the hole or slit spacing should be close to wavelength in the medium. In addition to the slit spacing being related to wavelength, the SPP intensity could also depend on the slit width as the shape of the slit could influence the $k_{d,s}$ distribution as well as the spacing. We might conjecture that a slit width of one-half the wavelength should be optimal. Then the spatial profile of the surface might resemble (very roughly) a sine wave of wavelength twice the slit width. This is a very simple argument. Simulations and/or theory should give us a better idea. The optimal spacing and width differs for the two interfaces because the SPP wavelength for the same frequency is different. For device applications the "business side" is the one with the Au-air interface, and we might want to suppress the SPP's on the glass side. However, our experimental measurements will involve measuring the interference of the SPP's on both sides of the film, thus here the SPP intensity on the glass side is of interest as well.

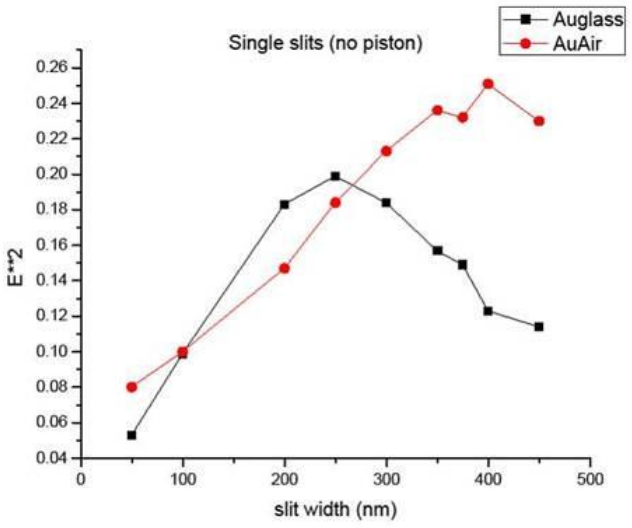

Fig.15: Dependence of the field intensity $|E_z|^2$ on the slit width of a single slit grating near the Au-glass and Au-air interfaces. The incident wave is normal to the surface of vacuum wavelength 780 nm (508 nm in the glass). The field intensities are taken 64 nm from the Au-glass and 48 nm from the Au-Air interfaces.

Fig. 15 gives the slit-width dependence, for a single slit, of the E_z field intensity near the Au - glass and Au - air interfaces. The peaks are at about 250 and 400 nm, respectively, for the two interfaces. These are not far off from our conjecture that the optimal width is half the wavelength in the glass or air medium. Note, however, that the maximum intensities there are 20-25% of the incident. This, we will see, is much less than what is obtained with multiple slits.

Fig. 16 gives the dependence of the field intensities near the Au interfaces on the grating period for a 4 slit grating with various slit widths. The expected resonant behavior with period occurs with peaks for the Au-glass interface near 450 nm and for the Au-air

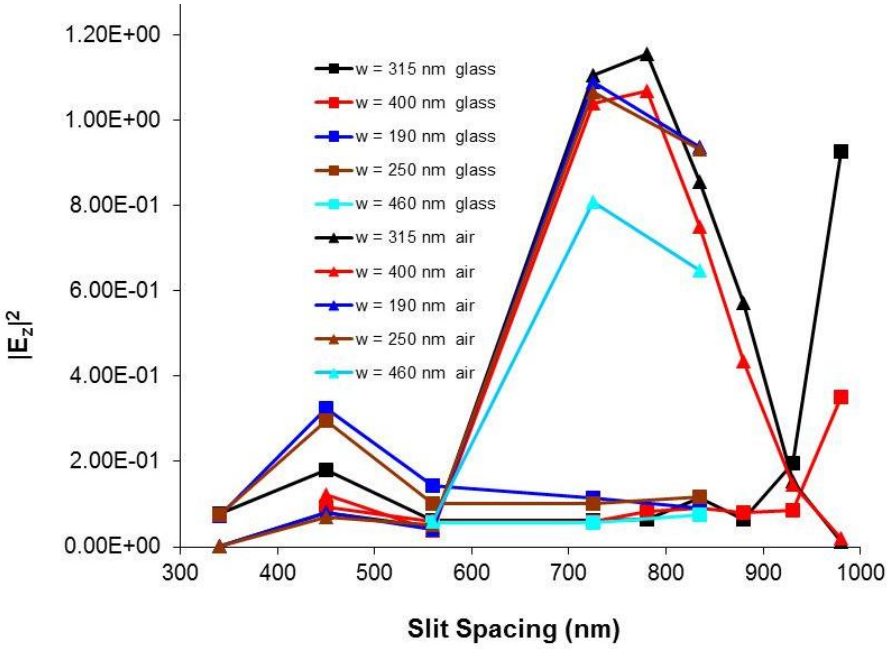

Fig. 16: Dependence of the field intensity $|E_z|^2$ on the period, or spacing and the slit width of a 4-slit grating at the same distances from the Au-glass and Au-air interfaces as Fig. 15. The incident wave is normal to the surface of vacuum wavelength 780 nm (508 nm in glass).

interface near 750 nm. There is also a resonant behavior on the glass side at about 980 nm spacing, which corresponds to the (*2,0*) mode of Eq. (3). The resonant intensities are about 0.4 times the incident for Au-glass for mode (*1,0*) at 450 nm spacing and 0.9 times the incident for the (*2,0*) mode at 980 nm, and 1.2 times the incident for Au-air at spacing 780 nm, which are several times the maximum single slit result. The optimal width parameters for launching SPP's on the air side are a slit-width of 315 nm and period 780 nm. In a device we would primarily be interested in the SPs only on the Au-air interface. In our experimental setup the SPP intensity is measured from an output slit in which case the SPs on both the Au-air and Au-glass interfaces interfere. At the optimal parameters for the air-Au interface this interference is fairly small but could have some effect. In practice a ~ 20 nm Ti or TiO_2 layer adhesion layer separates the Au and glass, and this suppresses the SPs on the Au-glass interface even more.

D.3 Surface Plasmon Waveguides

When one Au film is placed above another a SPP waveguide is formed. The wavelength and range is changed from that on a single flat surface. A finite length of such a waveguide can thus be used to change the phase of a SPP propagating in the waveguide as opposed to what it would be without the top film or with respect to another parallel waveguide with a different gap. We thus have a means of manipulating the interference emerging from a number of such waveguides, which is one main goal of our plasmonic holography effort. However, we must know in advance how the phase changes with waveguide geometry and also assess what losses may be suffered.

The material of the top film may alternatively be a dielectric or a metal. In the case of a Au bottom film, we found that a Au top film is most advantageous. In fact, dielectric top films cause the SPs to be scattered away from the surface. Therefore we will concentrate our discussion on Au-air-Au SPP waveguides. Our ultimate SPP Modulator, in fact, employs a flat bottom Au film and a top film consisting of various Au strips parallel in the direction of SPP propagation, i.e., a parallel series of SPP waveguides. We now, however, consider the properties of such waveguides infinitely extended in the lateral direction to understand their properties as a function of the air gap in between. Our waveguide setup, including the input slits and substrate appears schematically in Fig. 17.

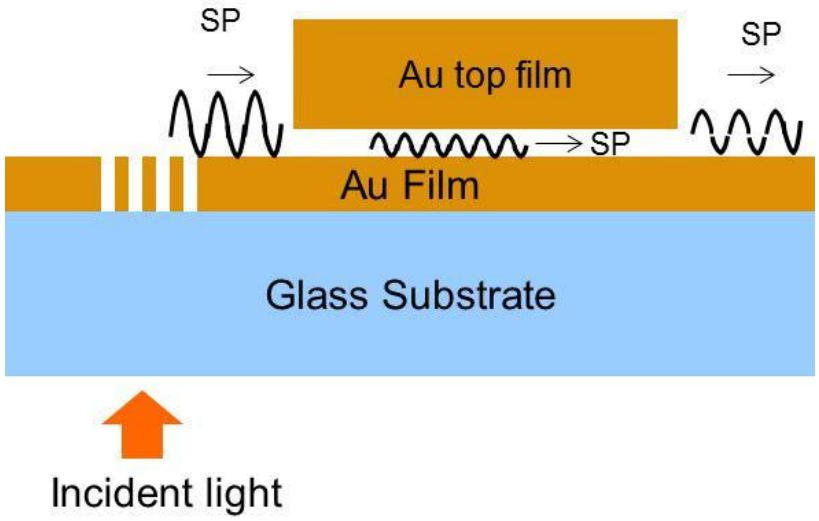

Fig. 17: Schematic SPP waveguide configuration. SPs are launched from the light incident on the input slits etched on the gold film atop a glass substrate. As the SPP propagates through the wave guide its wavelength and intensity are altered.

We now assess how the gap and length of the top film affects the intensity and phase of the emerging SPP. We first calculate the real and imaginary parts of the wave vector, and hence the wavelength, for SPs propagating between two infinitely extended, infinitely thick Au films as a function of the air gap. This can be done analytically with the results shown in Fig. 18 for incident light of vacuum wavelength 780 nm.

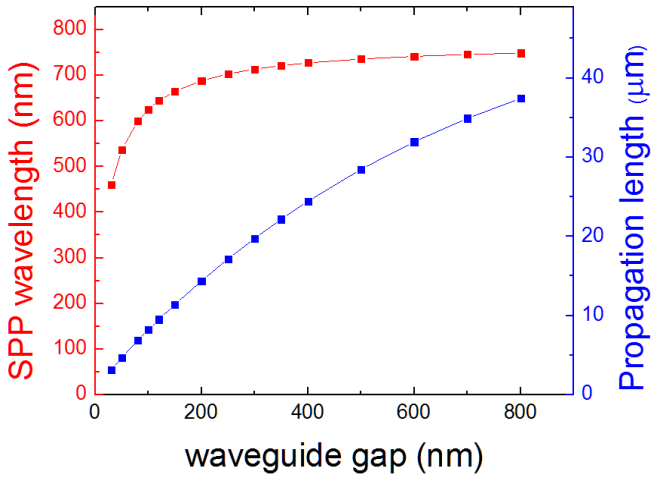

Fig. 18: SPP wavelength and propagation length as a function of the gap between infinite gold layers for 780 nm incident light.

Fig. 18 shows that the SPP wavelength and propagation length decrease as the gap narrows. The decreasing wavelength is desirable in that it will yield a more rapid change in phase (relative to a SPP on the flat surface) per unit length of waveguide. On the other hand losses are more severe for narrow gaps. The phase change emerging from such a waveguide is proportional to the length and the difference between the waveguide and without-waveguide wavelengths (the latter is about 762 nm). In terms of efficiency one figure of merit might be the phase change for, say, 50% losses. According to the results of Fig. 15 it turns out that gaps between 50 and 200 nm are the most efficient. Of course the thicknesses of the Au films and the length of the waveguide have some influence on the phase change and losses, but the main influence is essentially the dispersion relation indicated by Fig. 18.

The solid curves in Fig. 19 illustrate the transmission and phase change predicted by FDTD simulations for the setup of Fig. 17 with a 200 nm lower Au film and a 4 μm long thick (~3 μm) upper film. The dotted curves give the transmission and phase change when the thick

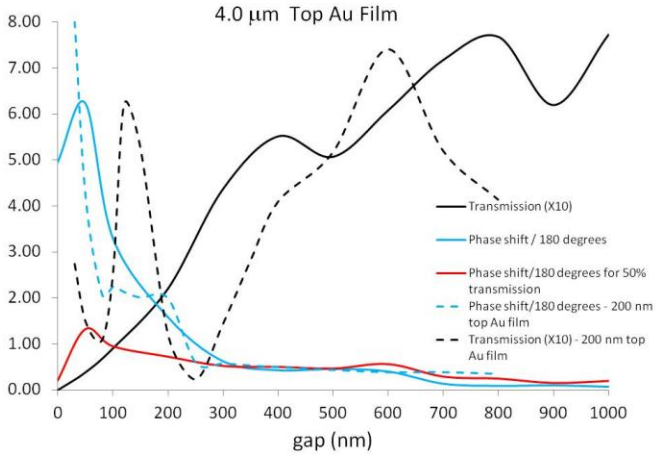

Fig. 19: SPP transmission and phase shift after traversing 4 μm of the waveguide of Fig. 17 where the bottom film has a thickness of 200 nm and the top a thickness of 3 μm (solid lines) or 200 nm (dashed lines).

upper film is replaced by a 200 nm film (which is what is used in our experiments). For the thick upper film the transmission generally increases with gap size and the phase shift decreases, as expected from Fig. 18. For the thin upper film there are large fluctuations from this trend, especially with respect to transmission, e.g., the peaks at 120 and 600 nm gaps. The difference between these sets of results is due to interference between the SPs propagating on the top of the top film with that propagating on the lower film. This follows from an examination of the transmission (and phase) as a function of the length of the wave guide.

Fig. 20 gives the transmission and phase as a function of waveguide length when the upper film is 200 nm thick and the gap is 120 nm. In earlier simulations with the thick upper film we found that to a good degree the phase linearly increased with length whereas transmission was approximately constant to within 20%. Now with the thin upper film the transmission is almost zero when the length is about 1700 nm with maxima near zero and 3400 nm. The maxima and minimum is the signature for interference between the SPP waves on the top film and the bottom film.

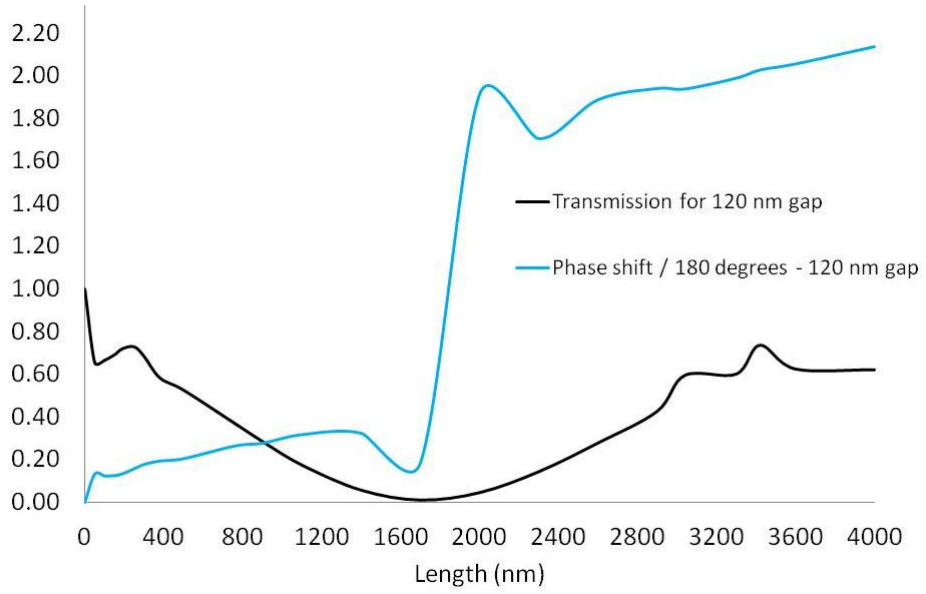

Fig. 20: The transmission and phase shift for a SPP waveguide with a 200 nm upper Au film and a gap of 120 nm as a function of length of the waveguide.

There is also almost a 360 degree jump in phase at the transmission minimum. The vertical e-folding distance for SPs of this frequency on a Au film is about 600 nm. Thus when the gap distance plus 200 nm upper film thickness is less than or comparable to this the SPs on the upper and lower films can interfere very strongly. This would not happen with the thick upper film because the incident SPP would have very little amplitude at the vertical displacement of the upper film. Given the dispersion results of Fig. 18 the difference in wavelength between SPs propagating in the gap and on a flat Au surface would imply a maximum-minimum separation of 2087 nm. The corresponding value from the simulations is 1600-1800 nm. The finite length of the waveguide and reflection and scattering at the ends may help account for the difference.

To fabricate devices with easily controllable phase and transmission properties we may wish to suppress the large fluctuations in Fig. 20. One way to do this is to insert a dielectric

region between the top film and the upper vacuum (or air). A 20 nm TiO_2 layer was previously used as an adhesion layer between the bottom gold film and glass substrate (see Fig. 17). This layer also effectively suppressed SPP waves on the glass-air interface. The following table, from analytic calculations, gives the range of SPs propagating on an infinite Au film covered by TiO_2 layers of various heights.

Table 1: Range of surface plasmons (vacuum wavelength 780 nm) for an infinite gold layer covered by various heights of TiO_2.

Height of TiO_2 Layer (nm)	Range of Surface Plasmons (μm)
0	42.8
5	31.9
10	23.6
20	12.5
30	6.1
40	2.9
50	1.6

Table 1 shows that the range of SPs can be seriously curtailed by a TiO_2 layer. The effectiveness of this layer in eliminating the interference effects in Figs. 19 and 20 depends on the length of the SPP waveguide. For example, if the waveguide has a length of 4 μm, as in our simulations, one would need a TiO_2 layer of > 35 μm. A 20 nm TiO_2 layer, however, would be sufficient for a 20 μm waveguide.

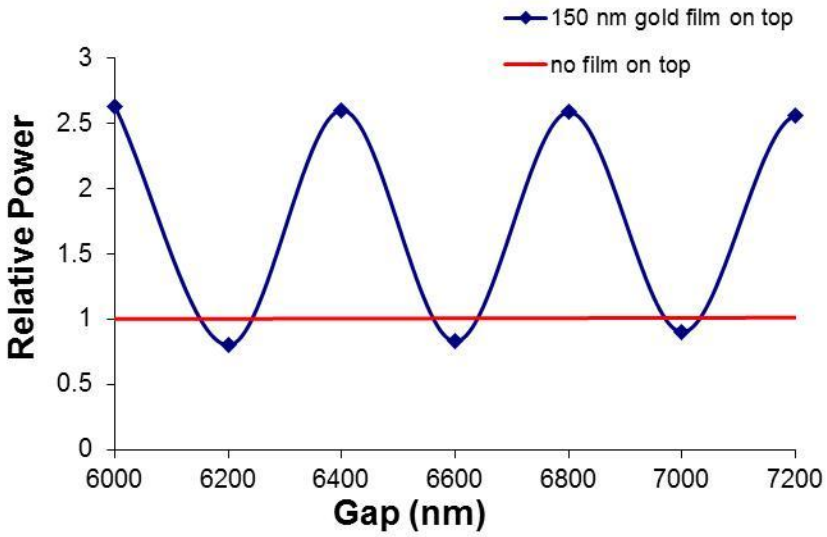

Fig. 21: The relative SPP power from FDTD simulation, as determined by the summed Poynting vector in the *z* direction from 0 to 600 nm above the Au surface, as a function of the gap between the Au surface and a top Au film of 150 nm thickness. The top film is placed directly above 6 input slits of width 380 nm and periodicity 830 nm and the plotted power is that relative to having no top film. The slits are illuminated from below as in Fig. 17.

D.4 Fabry-Perot Enhancement

While large gaps do not change the phase (much), they can function as Fabry-Perot (FP) resonators and greatly enhance the SPP intensity if top Au films are placed, say, directly above the input slits. The FP effect predicts that gap widths of ~ $n\lambda/2$ should be optimal. Fig. 21 illustrates the power converted to SPs from our FDTD simulations. These simulations confirm that the SPP intensity was enhanced by a factor of 2.5 for the optimal gap widths, which occur at a periodicity $\lambda/2$. A similar enhancement should also occur at the output slits making for an overall enhancement of a factor of 6. Experimental measurements are more favorable indicating an enhancement factor of 15. Details of our FP study appear in ref. [1].

One should note that the FP effect does not directly enhance SPP production. It enhances the radiant fields in the gap region that interact with the input slits, which in turn enhances SPP production. If there is a FP resonator above output slits a reverse enhancement occurs: The SPP interacts with the slits producing a radiant field that is enhanced by the FP effect, which in turn is transmitted through the output slits to be detected. The results in Fig. 21 represent the direct SPP production step but not the reconversion at the output slit that results in our experimental detection.

D.5 Role of Transverse and Longitudinal Slits

In the remainder of our theoretical and numerical analysis we will consider components of a Surface Plasmon Modulator (SPM), which we have also fabricated experimentally. A schematic diagram appears as Fig. 22.

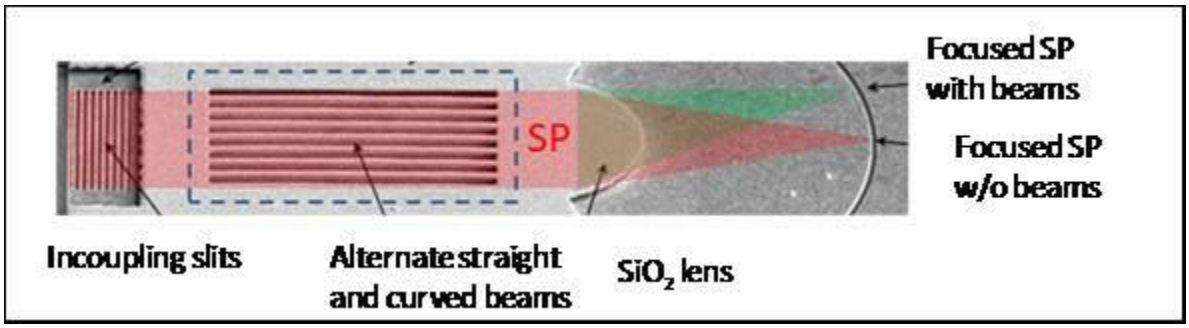

Fig. 22: Schematic top view of Surface Plasmon Modulator. The top gold film is 200 nm thick with alternating straight and curved beams that are 1000 nm wide and 20 μm long with 200 nm air gaps in between. The gap between the bottom and top films is 250 nm, and the SiO_2 lens has a radius of 8 μm and is on the same level as the air gap, and the curved beams dip 100 nm.

The main purpose of the alternate straight and curved beams, which are types of longitudinal slits and grooves in the top film, is to create phase differences between alternating sections of the wavefront in the SPM. This leads to a controllable diffraction pattern – a main goal of our plasmonic holography. Transverse slits are used for the incoupler of Fig. 22, for out couplers to measure the SPP radiation, and could also used to separate sections of devices like the SPM. Later in this report we will describe FDTD simulations of the SPM. In this section we mainly consider the effect of transverse and longitudinal slits and grooves on the propagation of SPs. First we consider the losses produced by a single slit.

Fig. 23 shows the loss of SPP (vacuum wavelength 732 nm) intensity, as predicted by FDTD simulation, as it transverses a single slit of various widths on a flat Au film. The SPP

incident on the slit is generated by an appropriate current source placed at $z = 0$ in the plot. The intensity, as measured by the longitudinal Poynting vector, S_z averaged over 600 nm (roughly the vertical decay length of the SPP field in the vacuum) above the gold film, normalized to the Poynting vector 3.1 μm from the current source when there is no gap. The current-launched SPP propagates on the Au film over a single transverse gap, of various widths, where the beginning of the gap is positioned 13.6 μm from the current source, as shown on the diagram at the top of the figure. Note that losses exist even when the gap is absent, with the SPP having a range of about 34 μm at this frequency. Losses occur here because the dielectric constant of Au at this frequency has an imaginary part, i.e., absorption.

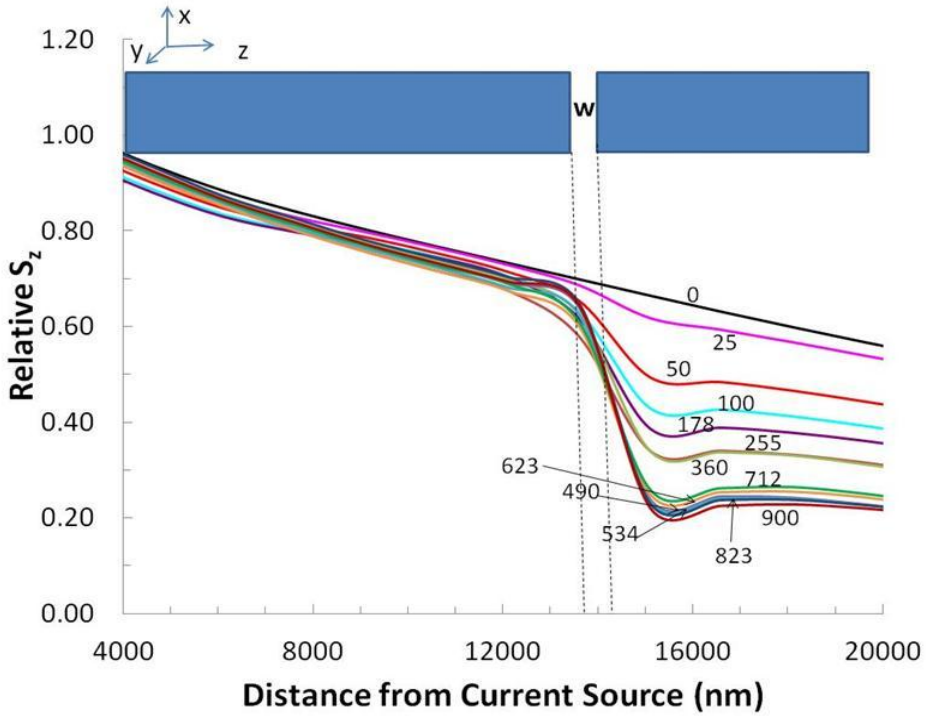

Fig. 23: Surface plasmon intensity, for various transverse gap widths, as measured by the averaged Poynting vector component S_z from zero to 600 nm above the Au surface, as a function of distance from the current source and gap width (w). The relative value of S_z is normalized to a value of 1.0 for the averaged Poynting vector 3.1 μm from the current source when there is no gap. The diagram at the top illustrates the gold film (filled in blue) relative to the z coordinate on the abscissa and the position of the gap at 13.6 μm from the current source. The Au film is 200 nm thick. The numbers labeling the curves are the widths of the gap in nanometers.

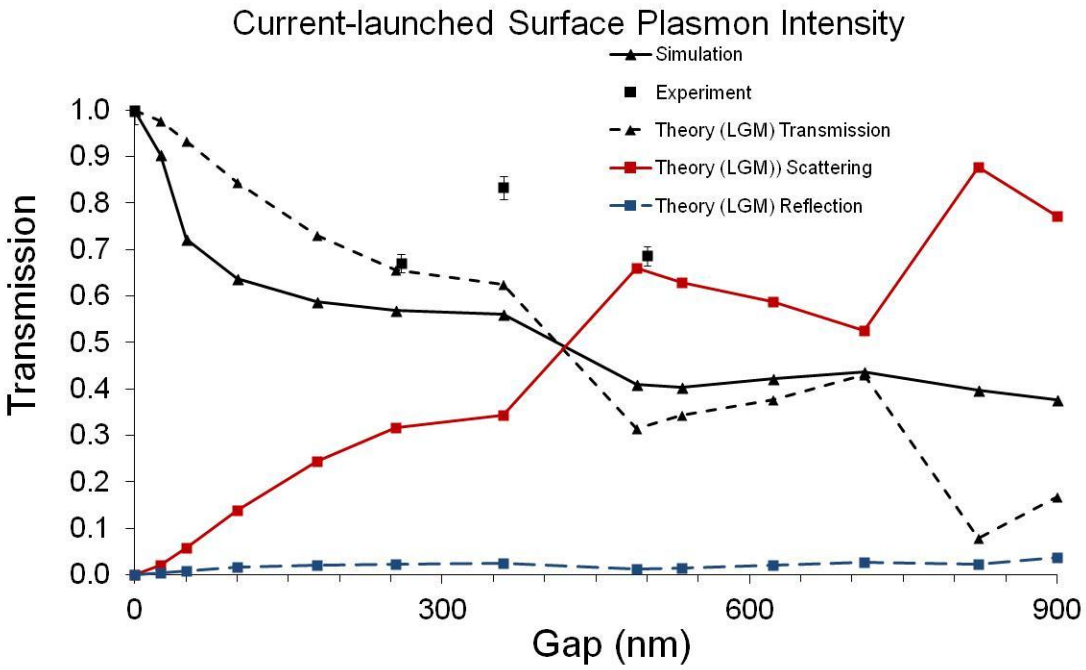

Fig. 24: Surface plasmon transmission across a transverse gap as a function of the gap width and our experimental results. The transmission is relative value of S_z, averaged vertically as described in Fig. 23, but normalized to a value of 1.0 for the averaged Poynting vector 16.6 μm from the current source when there is no gap. Results are also shown using the "tight-binding"-like theory of ref. [37] for the total SPP transmission, losses due to scattering of the electromagnetic energy from the SPPs into the vacuum at the gap, and the back-reflection of SPPs from the gap.

Fig. 24 gives the SPP transmission across the gap, as a function of gap width. The losses shown in Fig. 24 are those we attribute just to the gap itself, which includes the effects of reflection of SPPs and scattering of electromagnetic energy into the vacuum. We extract the transmission across the gap by comparing the Poynting vector S_z, averaged as in Fig. 23, at a point 2.9 μm after the beginning of the transverse gap (corresponding to the 16600 nm mark in Fig. 23) with that of the zero-gap result at the same point, which is thus normalized to unity. While the Poynting vector at this "observation point" contains the effects of further losses just from the propagation on the gold surface from the end of the gap to this observation point, the renormalization removes this effect that is not related to the gap itself. The simulations use a spatial mesh of (6 nm) [33] and a time step of 1/200 of the wave period. When compared with results of a (10 nm) [33] and time step of 1/120 of a period, the transmission increases by 3-5%. Thus we estimate the numerical error in the transmission as 3-5%. Fig. 24 also gives our corresponding experimental measurement of losses due to the gap. The setups of the simulation and experiment differ slightly – e.g., the gap in the simulation is 13.6 μm past the current source, whereas it is about 18 μm past the end of the grating in the experiment. Also the experiment measures intensity by measuring the light coming from the output slit (30 μm past the grating) whereas the simulation directly measures the SPP intensity by calculating the Poynting vector. To make a meaningful comparison we normalize the experimental intensities to the simulation result for the zero-width gap. This isolates the effect of the transmission across the gap and eliminates the effects of further losses because of the propagation distance between the gap and

the output slit and of the output slit itself (assuming that the output light intensity is proportional to the SPP intensity).

The simulation results in Figs. 23 and 24 exhibit two trends. As might be expected from scattering or diffraction arguments, initially the transmission rapidly decreases with gap size. However, as the gap approaches $\lambda_{SPP}/2$ (356 nm) the decrease quenches somewhat. From gap widths $\lambda_{SPP}/2$ to λ_{SPP} the trend repeats: a decrease in SPP intensity with w followed by a leveling off as the gap approaches λ_{SPP}. In fact, there is actually a local maximum near λ_{SPP}. Overall there is a general increase in losses with increasing w, but superimposed on this is a reflective interference effect of period $\lambda_{SPP}/2$ similar to that of a Fabry-Perot (FP) resonator. The experimental measurements, while generally indicating more transmission than the simulations, exhibit a similar alternating minima – maxima pattern. The minima are close to the minima in the simulations, but the maxima appear closer together than the simulations - at about 450 nm and 620 nm gaps, as opposed to about 355 nm (here actually a leveling in the decrease) and 720 nm in the simulations.

The general decrease of transmission with gap along with local maxima at $\sim n\lambda_{SPP}/2$ is argued qualitatively as follows. The SPP field has a longitudinal electric field and the finite conductivity at the relevant frequency yields a current flow. The coupling between two Au sides would then be capacitive (via Coulomb fields) and we would expect strong capacitive coupling for tiny gaps (typically $\lambda/8$ imperfections do little damage to the wave) and weakening for larger gaps. The SPP field also has transverse **E** and **H** components, and this part resembles an ordinary propagating plane wave in which case the gap would act like a Fabry-Perot (FP) resonator giving an alternating maximum – minimum structure with gap width.

F. López-Tejeira, F.J. García-Vidal, and L. Martín-Moreno [37] (which we refer to as LGM) study the interaction of SPs with slits or grooves using an analogy of the tight-binding method used in solid-state physics. (We will refer to this theory by the shorthand TB). Here the fields in the grooves are expanded in modes similar to those enclosed in perfect conductors, and the fields are matched at the top and bottom boundaries of the metal to calculate the fields in all space. The dotted curves in Fig. 24 give the results of this approach for SPs propagating on top of a 200 nm gold film traversing a single gap of various widths. The losses in this approach due to reflection and scattering to the vacuum also appear in the figure. While there are some differences between the TB results and simulations (e.g., the simulations show less transmission for small gaps) the trends are in good agreement, especially for the muted FP effect mentioned above. In the usual FP effect minimum reflection and maximum transmission occurs at half wavelengths. In our situation the reflection is evidently always small (Fig. 23), and losses are almost entirely due to scattering of the SPs into the upper vacuum, which is minimized at gaps of multiples of half wavelengths. The simulations, theory, and experiments all resemble the usual FP case in that transmission minima occur near odd multiples of quarter wavelengths.

The properties of series of slits or grooves are also of interest. Series of transverse slits or grooves are used for the input slits of the SPM (Fig. 21). More input slits enhance the SPP intensity simply because they take in more incident radiation. But this is limited, as we shall see, by the reduced range of a multi-slit array, which comes about from the scattering of SPs into the vacuum and back reflection. Longitudinal grooves/slits on the same device on the upper film (e.g., the "beams") are used for phase manipulation, and again a reduced SPP range is a limiting factor. We first consider series of transverse slits.

Just as the wavelength and range in SPs is altered by a SPP waveguide, they are also altered in a region of periodic slits. These can be calculated by the LGM method. Doing this we immediately find that ranges are markedly reduced but the wavelengths only slightly changed. Therefore they are not competitive with the waveguides (of gaps < 250 nm) for changing phases. However slit or groove arrays can be optimized as in-couplers. S.T. Koev, A. Agrawal, H.J. Lezec, and V. Aksyuk [25] (referred to as KALA) suggest that the incoupling efficiency is a

sensitive function of the range of the SPs in the grooved region, with the optimal coupling occurring when the range associated with losses from scattering at the grooves is equal to the range associated with losses on a corresponding flat surface. They also measure the ranges and incoupling efficiencies for various groove widths and heights. The results of the range measurements [25] and LGM predictions are shown in Fig. 25. The agreement is rather good except for the theory predicting longer ranges than experiment on the large groove height end. This encourages the use of the rather computationally simple LGM theory in assessing the effects of groove geometry.

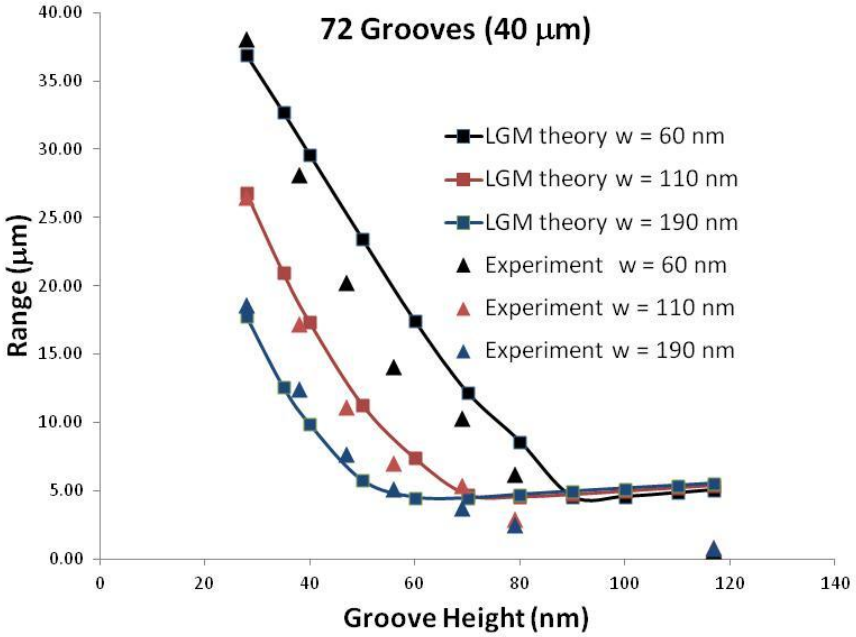

Fig. 25: The e-folding range of SPs, with frequency corresponding to 780 nm vacuum wavelength, propagating in a region of grooves spaced at 560 nm, as calculated by the TB theory (LGM) of ref. [37] and measured in ref. [25], as functions of groove width and height. For reference the range for these SPs on a flat Au surface is 43.0 nm. The grooved region used in the theory and experiment is 40 μm long (72 grooves).

In Fig. 25 the groove spacing is 560 nm, at which periodicity, as stated in ref. [25], diffraction to higher orders is eliminated. The SPP range at this frequency on a flat Au surface is 43.0 μm, meaning that the ideal range for incoupling in Fig. 24 occurs when the range is 21.5 μm because there the ranges produced by the scattering of the grooves and that on a flat surface are equal. The calculations and theory are for illumination on the topside of the grooves, which is opposite that illustrated in Fig. 17, but used in the latest versions of the modulator.

The heart of the SPM (Fig. 22) is the longitudinal beams that vary the phase across the wave front. So we now consider the effect of longitudinal grooves and slits on SPP propagation. Fig. 26 shows the SPP intensity as it propagates along a series of longitudinal gold strips separated by air gaps as shown in the diagram at the top of the figure. In our experimental

arrangement we usually employ about 8 or 9 strips of width 0.75 μm (as opposed to three shown in the figure). The simulations employ periodic boundary conditions in the *x* direction, which corresponds to an infinite series of such strips (and gaps). The SPs in the simulation are current-launched, and the spatial grid used is (10 nm) [33] and the time step 1/120 of a period. By comparison to simulations with a (15 nm) [33] grid, we estimate that the error in the ranges in the inset of Fig. 26 at 10-15%. The strip structure starts 3.6 μm from the end of the launching current region and extends 11 μm, as in the experiment, at which point an ungrooved Au film resumes. Extending the grooved film further to the end of the 30 μm box has negligible effect on the curves of Fig. 26.

To a good degree all the curves in Fig. 26 have exponential decay, even when there is no gap, as previously discussed. The inset of Fig. 26 gives the range or propagation length, as a function of gap size, based on a least squares fit, for the five gap sizes considered. The losses here may be described in terms of scattering from the strip structure and modifications of the SPP propagation vector due to the periodic strip structure, as illustrated by the agreement with the theoretical curve (labeled "TB") in the inset, as will be described below. The inset to Fig. 26 also shows results of experimental measurements for a 9 strip SPP waveguide. The experimental range is extracted from the transmission data at the output slit taking into account that the strip region is 11 μm long. As with Fig. 17 the experimental measurements have been normalized to simulation results for the zero gap case, and thus the ranges in the inset correctly shows the *difference* in ranges between the simulations and experiment (and also difference between the finite gap cases and zero gap).

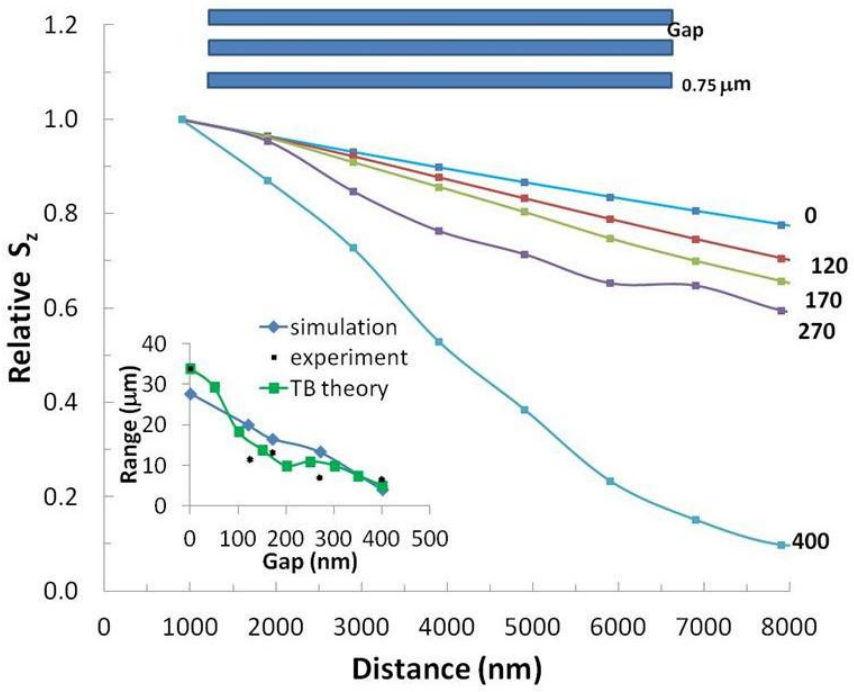

Fig. 26: Surface plasmon intensity, for current launched SPs, as measured by the summed Poynting vector component S_z from zero to 600 nm above the Au surface, as a function of distance from the beginning of a striped region and gap width. The number associated with each curve gives the gap width in nm, whereas the Au strip width is always 0.75 μm. The position of the gap is illustrated at the top of the figure with the filled region indicating the Au surface. The inset gives the e-folding range as a function of gap width (see text) from simulations and the theory of LGM – labeled "TB theory". Error bars of ± 3% (too small to be seen) are assigned to the experimental points in the inset.

Generally there is good agreement between experiment, theory, and simulation for the overall decrease of range with gap size. Simulations give a fairly uniform decrease in range with gap width, while the theory and experiment indicate some maximum – minimum structure (inset, Fig. 26). However the positions of the maxima and minima in theory and experiment differ. For device applications we would like ranges > 15 μm, which indicates that gaps up to about 150 nm could be tolerated. One reason for the disagreement between simulations and experiment could be due to the simulation employing an infinite number of strips while the experiment employs a finite number (8 or 9). The finite number of strips used in the experiment would necessarily lead to a somewhat shorter SPP range than in the simulation. The simulations also indicate a range of about 28 μm for the ungrooved case compared to a range of 33 μm gotten from the imaginary part of the SPP wave number at 732 nm for a flat Au film.

Ebbesen et al. [27] have discussed the usefulness of metal strips as SPP waveguides. Previous treatments [39] of SPP propagation on strips have mainly concentrated on a single metal strip, whereas our case employs multiple (e.g., 8) strips. The "tight binding" theory of LGM does not directly address longitudinal gaps but restricts itself to SPs normally incident on transverse gaps. We extend this approach as follows: We use the methods of ref. [37] to calculate the transmission and reflection of SPs normally incident on a series of n transverse gaps (usually n = 8) with the same width and spacing as the longitudinal gaps we are considering. We then approximate the problem in a 2D way where an electromagnetic (em) wave of wave number k_{SP} and frequency ω in the metallic regions encounters a dielectric region with a complex dielectric constant and width $(n-1)\,d + a$, where a is the gap width of the slits and d is the periodicity of the slits. The effective dielectric constant in the metallic regions of width $d - a$ is determined by k_{SP} and ω, and we calculate what effective complex dielectric constant in the region of width $(n-1)\,d + a$ would account for the transmission and reflection results of the TB theory. (This has a significant imaginary part since most of the losses are due to scattering, not reflection, and this is treated as an effective absorption). We then estimate a typical change in the SPP propagation vector due to interaction with the series of slits represented by a corresponding series of alternating dielectric regions, which is in the x direction, i.e., normal to the slits. These alternating regions consist of a metallic region $d - a$ = 0.75μm wide followed by a region of width a region $(n-1)\,d + a$ of its dielectric constant. The change in the wave number can have both real and imaginary parts where the latter will correspond to the attenuation the "diverted" SPP suffers as it propagates in the direction perpendicular to the slits (as well as parallel).

One way to estimate the change in the SPP propagation vector $\Delta\boldsymbol{k}_{SP}$, appropriate for a periodic collection of alternating (complex) dielectric regions, is to solve for Bloch states. In this case one obtains both real and imaginary parts of the Bloch q vector (which here only has an x component). The real part of q, which we look for in the first Brillouin zone, indicates the typical displacement of the wave vector in the x direction, and the imaginary part gives the decay constant of the SPP wave amplitude in the x direction. The overall decay constant κ for the SPP intensity I as measured along the principal propagation direction along the z axis is then given by

$$\kappa = -\frac{1}{I}\frac{dI}{dz} = -\frac{1}{I}\frac{\partial I}{\partial x}\frac{dx}{dz} - \frac{1}{I}\frac{\partial I}{\partial z} = 2Im(q)\frac{Re(q)}{Re(k_{SP})} + 2Im(k_{SP}), \qquad (4)$$

where the factor two appears because of converting decay constants for the amplitude to that for the intensity. The e-folding range is simply $1/\kappa$. With this ansatz the $Re(q)$ ranges from 0.00038 nm^{-1} for 50 nm air gaps to 0.0026 nm^{-1} for 400 nm gaps, and $Im(q)$ ranges from 0.000055 nm^{-1} to

0.00029 nm^{-1} over the same interval of gap widths, compared to $k_{SP} = 0.00882 + 0.000015\,i\ nm^{-1}$. The ranges obtained from Eq. (4) appear in curve labeled "TB theory" in the inset of Fig. 26. The theoretical results are in good agreement at the experimental points (which have about ± 3% error bars) and with results obtained from simulations, except the simulation results appear to be slightly too low for the narrowest gaps. Again the LGM approach gives accurate results with little computational effort.

D.6 Surface Plasmon Phase Modulator Simulations

We now consider the phase modulation and losses from the SPM of Fig. 22. From the previous results we have an idea on the performance of the various components, so now we have a chance to assess the modulator as a whole. We approach this assessment in two phases. The first considers the role of the alternate straight and curved beams essentially in isolation, while the second looks at the performance of the full SPM.

We first consider the SPM of Fig. 22, but without the focusing SiO_2 lens, and with the alternate beams and the gold films extended indefinitely in the lateral (i.e., *x*) direction. We also use current-launched SPs to eliminate the input slits and to isolate the effect of SPs impinging on the region of the beams. The beams in Fig. 22 are 1.0 μm wide with 200 nm air spaces in between. The gap between the bottom film and the straight beams is 250 nm (as in the fabricated devices) and the top beams are 200 nm thick and 20 μm long. The curved beams are configured like the straight beams except they have a parabolic shape lengthwise with a dip of 100 nm midway. The simulations have a computational volume that extends 2400 nm laterally (a unit cell in the *x* direction consisting of one straight beam, one curved beam, and two air gaps), 72 μm in the *z* direction, with the Au film ending at 64 μm, and 3.0 μm vertically (*y* direction). Perfectly Matched Layer (PML) boundary conditions [36] at the *y* and *z* extremities minimize artificial reflections from the computational box.

Fig. 27 gives the SPP intensity, as determined by the total S_z summed up to 250 nm above the bottom Au film over the full lateral extent of the film, as a function of the *z* distance from the beginning of the beam region. This is normalized to 1.0 at the beginning of this region. The overall effective SPP range in the beam region is 9.1 μm, similar to the results in Fig. 26.

The main purpose of the alternate straight and curved beams in the SPM is to create a phase difference across the SPP wavefront. Fig. 28gives the phase angle of H_x across the unit cell of one curved beam and one straight beam and two separating air gaps at various longitudinal distances (referred to the beginning of the beam region). The phase profiles shown are at 8 μm, i.e., near the middle of the beams, at 28 μm, i.e., 8 μm past the end of the beams, and at 48 μm, well past the beam region. The maximum phase difference between the beams is about 220 degrees at 8 μm, 190 degrees at 28 μm, and 150 degrees at 48 μm. As might be expected the transition in phase is sharpest in the beam region, and the phase difference decreases and the transition smoothens as one proceeds further past the end of the beams. This "smearing" of phase differences is likely due to the diffraction and scattering produced by the beams. These simulation results demonstrate that the SPM design of Fig. 22 is capable of producing phase difference of the order of π radians across distances of the wavefront of order of the wavelength.

The principal effect of the phase differences across the wave front should be some sort of diffraction pattern. Fig. 29 gives a 3D plot of the SPP intensity, as determined by the Poynting vector in the direction of SPP propagation, S_z, summed over 250 nm above the bottom Au film, as a function of *x* and *z*.

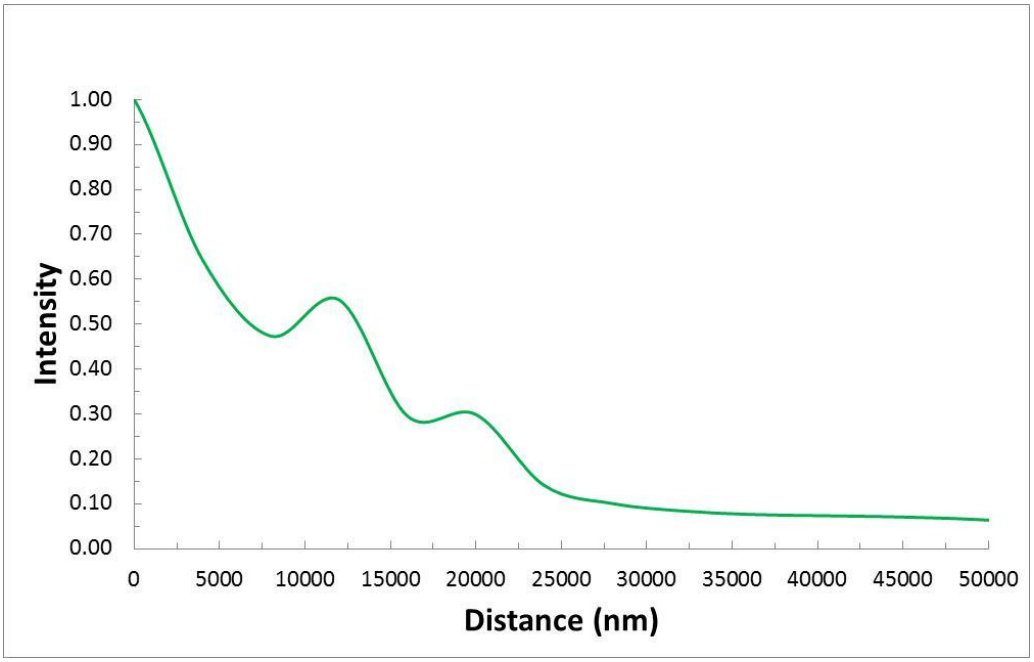

Fig. 27: The overall SPP intensity as it propagates along the beam region (and beyond) of the SPM of Fig. 17 as modified by the description in the text. The intensity is normalized to that at the entrance to the beam region.

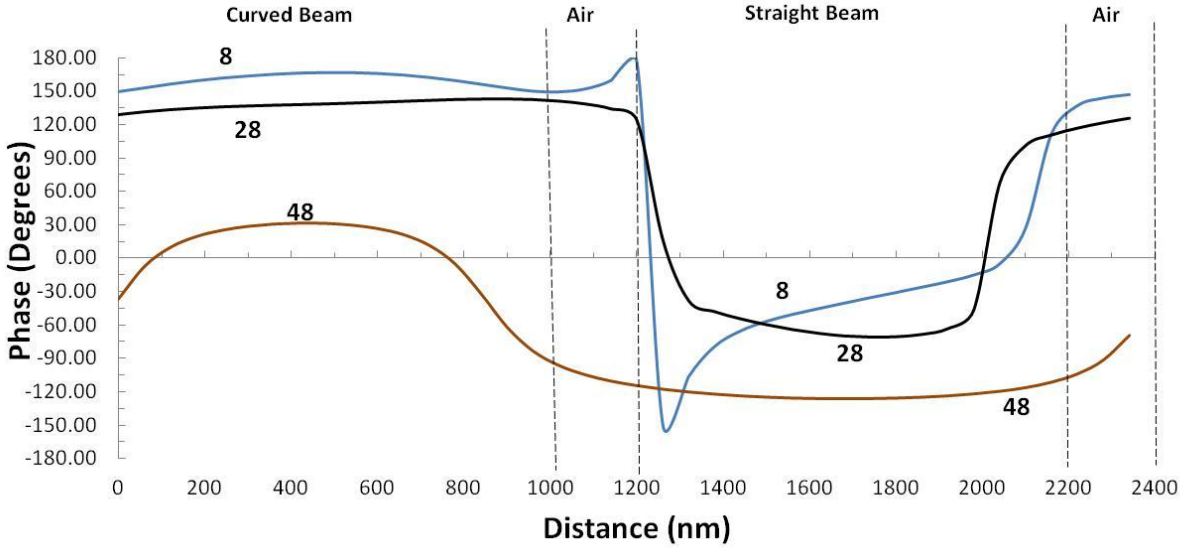

Fig. 28: The phase of H_x 60 nm above the bottom Au surface laterally across the unit cell (x direction) for three different distances from the beginning of the beam region of Fig. 22. The numbers labeling the curves indicate the distance in μm from the beginning of the beam region. The beam region extends 20 μm. Laterally, the regions corresponding to the curved beam, the straight beam, and the air gaps in between are indicated.

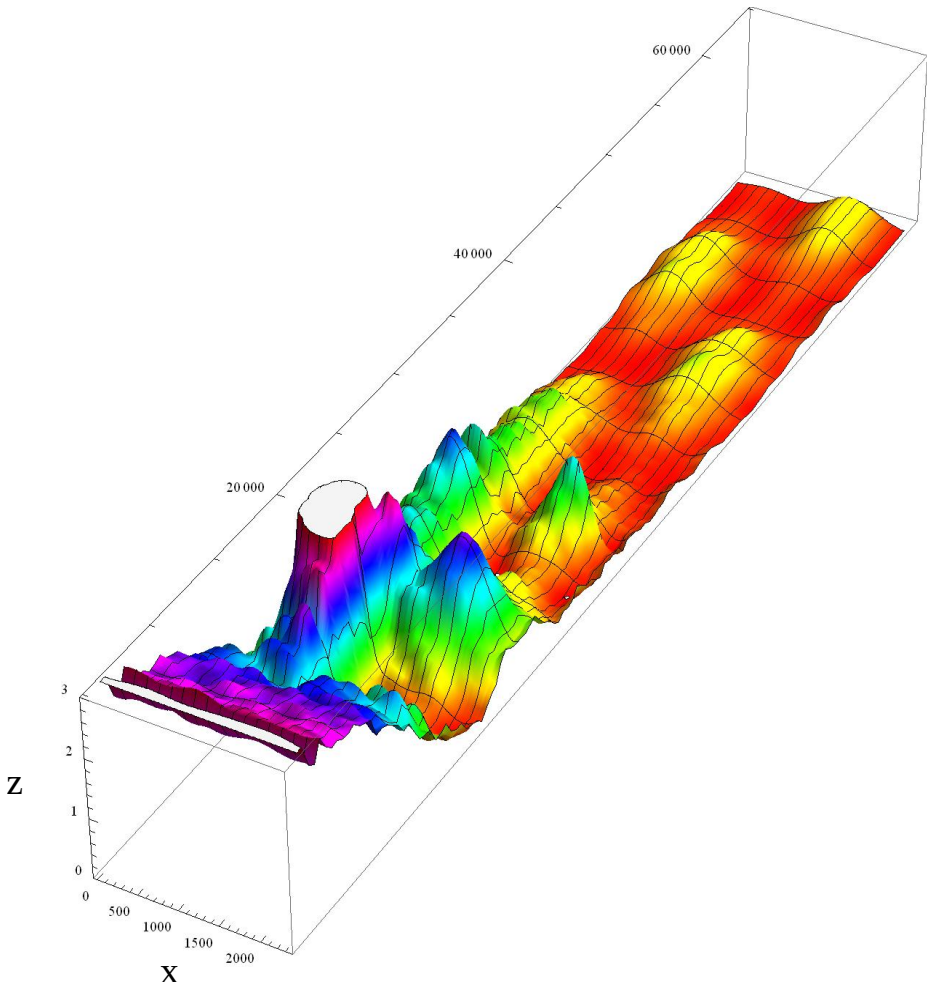

Fig. 29: Three dimensional plot of the x and z dependence of the SPP intensity as measured by S_z summed over 250 nm above the bottom Au film. The x and z axes labels are in nm, and the intensity is in arbitrary units. The beam region is z = 12000 nm to z = 32000 nm. The curved beams extend from x = 0 nm to x = 1000 nm, and the straight beams from x = 1200 nm to x = 2200 nm.

In Fig. 29, z coordinates between 12000 and 32000 nm define the beam region and at $z >$ 32000 nm the SPs are propagating on a bare Au film. The distinct maxima that appear for $z >$ 32000 show the near- and intermediate-field diffraction pattern. This result indicates that the alternating curved and straight beam design used in the SPM has the capability of producing a controlled diffraction pattern (controlled by the size, shape, and spacing of the beams), which effectively in the far-field controls the direction of the SPP "jet".

The fabricated SPM differs from that employed in Figs. 27-29 in that there are a finite number of beams (actually eight in our actual device) and the presence of an SiO_2 lens just after the beam region. (See Fig. 22). In addition to the SiO_2 lens, there are also SiO_2 posts of 2 μm lengths supporting the ends of the beams. Simulations without the beams or the posts but just with the SiO_2 lens (of radius 8 μm) indicate a focal spot centered about 25 μm past the beginning of the lens. This is close to the focal point one would predict from a lens of this shape when the index of refraction changes by that indicated from the change of the real part of the wave number

for SPs propagating along a Au-SiO_2 interface to a Au-air interface (i.e., $n_{Au\text{-}SiO2} / n_{Au\text{-}air} = 1.54$), which would be ~30 μm. This latter number is really the small incident angle limit and since the lens is cylindrical there is some aberration that would smear out and reduce the distance of the center of the focal spot somewhat.

What is really of interest is how the SPM varies the phase across the wavefront and losses under the beams. Fig. 30 plots the relative phase and intensity profiles across the beam front in the beam region at 6 and 18 μm from the beginning of the beams for the SPM of Fig. 22.

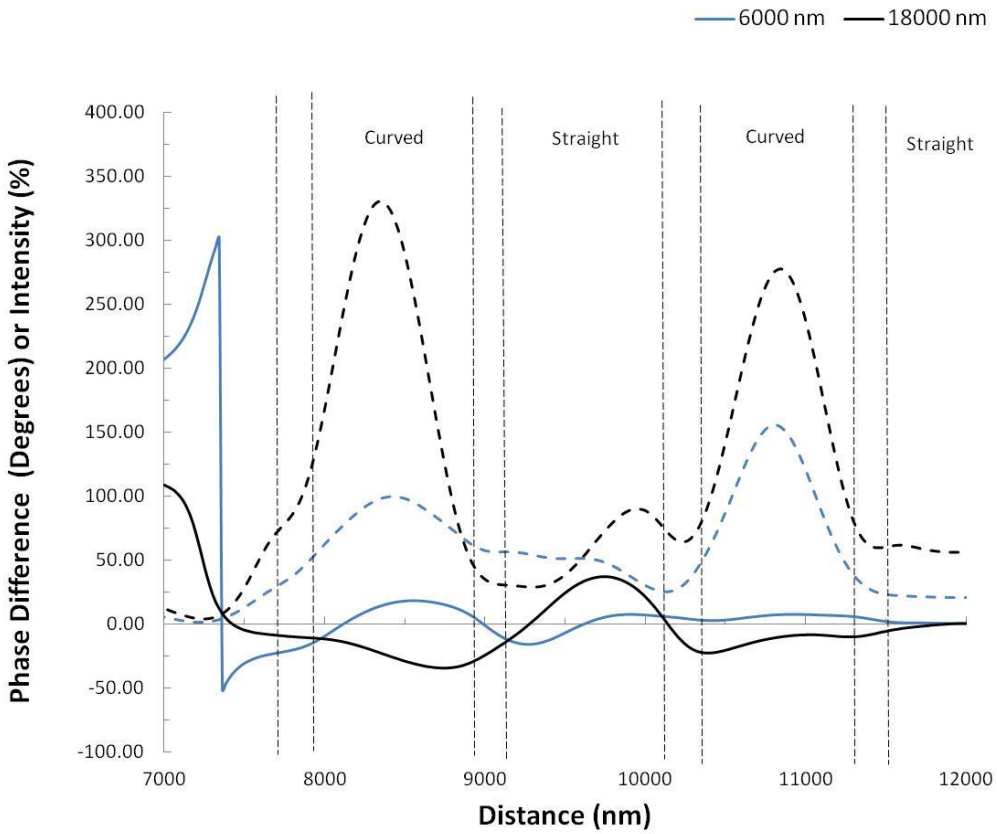

Fig. 30: The relative phase (solid lines) and intensity profiles (dashed lines) of H_x 50 nm above the bottom Au surface across the wavefront in the beam region for the SPM of Fig. 22. The phase difference is referenced to the phase at the center of the central straight beam (at 12000 nm in this figure) for the given distance from the beginning of the beams, and the intensity (in percents) is relative to that at the center of the central straight beam 2μm from the beginning of the beam region. A half profile is shown as the H_x field is symmetric about the longitudinal center line (x = 12000 nm in the figure). The positions of the curved and straight beams are indicated and the distances on the abscissa indicate the distance from the edge of the actual SPM.

The maximum phase difference between a curved and straight beam segment of the wavefront is about 40 degrees at 6 μm into the beam region and about 70 degrees at 18 μm (i.e., 2 μm from the end). These are not as large phase differences as for the idealized infinitely periodic beams of Figs. 27-29, but still a significant phase difference. The losses are similar. The intensities are significantly larger under the curved beams. This was also true for the periodic beams as one can see in Fig. 29 that there is more intensity in the beam region (z = 12000 to 32000 nm) under the curved beam (x = 0 to 1000 nm) than under the straight beam (x = 1200 to

2200 nm). Unfortunately this hampers the performance somewhat as the phase difference would play the largest role in diffracting the SPP jet when the intensities are roughly equal.

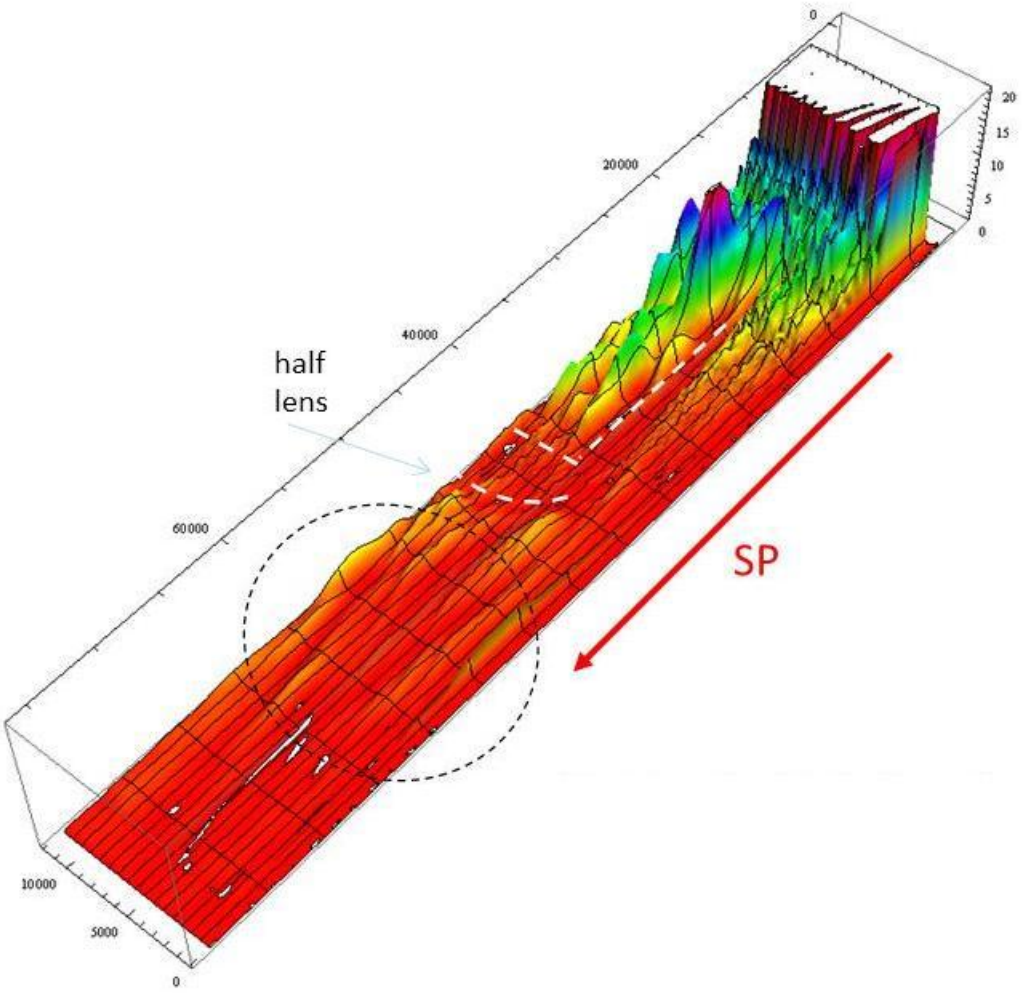

Fig. 31: 3D simulation of the SPP intensity from the modulator of Fig. 22. The beam region and SiO_2 lens region are outlined by dotted lines. The region in the dotted circle is explained in the text. Only half the width is shown because the intensities are symmetric about the center line at 12000 nm in the figure.

Fig. 31 gives a 3D plot of the SPP intensity for the SPM as measured by the total S_z summed up to 500 nm above the bottom Au surface. Although more subtle than in Fig. 27, multiple peaks are seen past the modulator and lens (note circled region). The intensity distribution after the lens may explain the multiple peaks of out-coupled light seen in the experimental data and the combination of effects coming from the phase changes in the modulator (i.e., beam region) and focusing from the lens. The fact that the contrast in intensity here is less than for the idealized structure (Fig. 29) is a consequence of the smaller phase differences between curved and straight beam sections of the wavefront (compare Figs. 28 and 30).

D.7 Concluding Remarks on Simulation and Theory

Our simulation and theoretical investigations of the SPM and related components has helped determine the acceptable parameter space for our device as well as plasmonic devices in the future that may employ similar components. Our main goal has been to manipulate the spatial variation of the SPP phase while maximizing SPP intensity. We have determined the optimal way to launch SPs using multiple input slits. The optimal spacing (for normal incidence) is equal to the SPP wavelength with slit widths roughly half the SPP wavelength. Placing a second Au film as a Fabry-Perot resonator can enhance the SPP intensity by an order of magnitude. The optimal air gap in the SPP waveguide is 50-200 nm as gaps smaller will lead to unacceptable losses, while larger gaps will not yield much of a phase shift. Thin upper films hamper the control of the phase (and intensity) because of interference of SPs on the upper film, but this can be mollified by coating the upper film with a dielectric such as TiO_2. We can significantly vary the phase across the wavefront by employing, e.g., alternating straight and curved "beams" to effectively vary the gap size of neighboring "waveguides" across the wavefront. Our study of the behavior of SPs propagating on longitudinal strips has shown that we should not have gaps much larger than 200 nm between such beams or else losses may be unacceptable. Finally our investigation of both idealized and realistic SPPMs has confirmed that phase differences of 90 degrees or more are obtainable between pairs of such beams, but a disparity in intensity under the beams may hamper the modulators performance. If, as likely, the disparity comes from different interference with SPs atop the upper film, the cure may be to coat the upper film with something like TiO_2 to suppress the upper SPs. Also a wider modulator may help as it would more resemble the idealized version assessed in Figs. 27-29 as these give larger phase differences.

E. Student Training

Students receiving training during the period of AFOSR support were: visiting graduate student Siim Pikker from the University of Tartu (Tartu, Estonia) and undergraduate independent-study students from Rutgers: Timothy Su, Katherine Sytwu, Philip Lubik, David Kolchmeyer and Harsh Shah.

The integration of research and education was achieved through active participation in design, development and testing of the novel nano-photonics devices described in this report and provided an especially broad training that should equip students for careers in industry, the national laboratories, or academia. Siim, Timothy and Katherine were involved in data analysis, computer design and optical characterization of plasmonic devices nano-fabricated at the NIST CNST.

PI has made a special effort to attract women and under-represented minorities to research. Since 2010, PIs have supervised seven undergraduate students; Philip Lubik has had his work presented at national meetings, he and David Kolchmeyer are coauthors on three published and forthcoming research papers. Katherine Sytwu, a female undergraduate, is excelling in research in the field of non-linear plasmonics.

Mentoring postdocs and junior research associates in the group, including Alexander Ignatov and Verner Thorsmolle, comprised in-depth scientific discussions on their projects. Postdocs and research associates were attached as collaborators on research projects conducted by undergraduate students in the group; they were involved in preparation of publications, posters and conference presentations.

F. Conclusion

The investigators have designed, numerically simulated, developed a nanofabrication process for and demonstrated functional elements of prototype Surface Plasmon Modulator (SPM) micro-electromechanical systems (MEMS) designed to manipulate and shape surface plasmon polariton (SPP) wavefronts. The SPM was composed of a double gold film plasmonic slot waveguide with an in-coupler grating, electrically actuated doubly clamped free floating gold nano-beams, an SPP focusing lens and an out-coupler slit. Gold nano-beams were chosen for the phase retarding modulators due to it's high dielectric constant. In prior art, moving Au films have not been used in MEMS devices and therefore substantial developmental work had to be performed.

Finite difference time domain numerical simulations were performed to design devices that allow manipulation of the SPP phase across a wavefront, while at the same time enhancing the intensity and/or minimizing losses as the SPP wave propagates. The simulations explored several device aspects including: design of electrically actuated Au nano-beams capable of oscillation at 1 MHz with submicron amplitudes. 1) efficient production of SPP waves from gratings; 2) changes in phase and resulting losses from SPP waveguides characterized by having SPPs propagate between two gold films; 3) enhancement of SPP intensity by using Fabry-Perot resonators; 4) propagation of SPPs in the presence of transverse and longitudinal slits (beams or electrodes) on either top or bottom of a plasmonic waveguide; 5) SPP focusing by a dielectric lens and 6) integration of beams, lenses and slits into an SPM device.

A process was developed to nanofabricate prototype SPMs. Critical processing steps achieved were: 1) deposition of an Au/SiO2/Au stack using TiO2 as adhesion layer for Au to SiO2; 2) focused ion beam (FIB) lithographic patterning of free floating Au MEMS nano-beams, in-coupler gratings, plasmonic lens and out-coupler window/slits; 3) use of liquid oxide etch to create free floating Au nano-beams; 4) use of CO2 critical drying to prevent Au nano-beams from sticking down after liquid etch; 5) FIB fabrication of plasmonic devices for SPPs decay measurements after traversing longitudinal and transverse slits; 6) fabrication of Au coated Si cantilevered pistons for phase interference measurements and 7) potential conversion to parallel processing with e-beam lithography. Test structures were fabricated with 150 nm features.

Several SPM elements were demonstrated that are necessary for achieving an operational SPM including: 1) simultaneous electrical actuation of six free floating Au beams at 1 MHz with stroboscopic interferometric profilometry; 2) light coupling into an Au SPP slot waveguide via grating coupling; 3) SPP propagation through the plasmonic slot waveguide, including reflection and transmission through SiO2 beam supports and lens; 4) detection of focused out-coupled light by a two dimensional dielectric SPP lens; 5) detection of diffractive changes in out-coupled light with SPP modulator beam motion; 6) SPP decay measurements after traversing longitudinal and transverse slits and 7) enhanced plasmonic light coupling with a nano-structured Fabry-Perot resonator [1].

Undergraduate, graduate and post-doctoral students received training in the Rutgers laser lab during the period of AFOSR support. Research and education integration was achieved through active participation in design, development, testing and data analysis of the novel nano-photonics devices described in this report.

References

[1] Dennis B.S., Aksyuk V., Haftel M., Koev S., Blumberg G. Enhanced coupling between light and surface plasmons by nano-structured Fabry-Perot resonator. J. of Applied Phys. **110**, 066102 (2011).

[2] D.K. Gramotnev and S.I. Bozhevolnyi, Plasmonics beyond the diffraction limit, Nature Photonics **4** 83 (2010).

[3] Egorov D., Dennis B.S., Blumberg G., Haftel M.I. Two-dimensional control of surface plasmons emitted from arrays of subwavelength apertures. Phys. Rev. **B70**, 033404 (2004).

[4] Optical Routers Based on Surface Plasmons, G. Blumberg, B.S. Dennis and D.M. Egorov, US Patent #7,039,315, issued April 11 and May 2, 2006.

[5] Optical Routers Based on Surface Plasmons, G. Blumberg, B.S. Dennis and D.M. Egorov, US Patent #7,039,277, issued April 11 and May 2, 2006.

[6] Optical Routers Based on Surface Plasmons, G. Blumberg, B.S. Dennis and D.M. Egorov, US Patent #7,027,689, issued April 11, 2006.

[7] Optical Routers Based on Surface Plasmons, G. Blumberg, B.S. Dennis and D.M. Egorov, EP1445632, issued August 11, 2004.

[8] Surface plasmon-based optical router for converting electric signal to optical signal and optical signal to electric signal, G. Blumberg, B.S. Dennis and D.M. Egorov, KR1020040067790, issued April 11 and July 7, 2004.

[9] Plasmonic Optics for Plasmonic Circuits. G. Blumberg and V. Aksyuk. U.S. Patent application 20090142016, filed on June 4, 2009.

[10] H. Raether. Surface plasmons on smooth and rough surfaces and on gratings. (Springer-Verlag, Berlin, 1988).

[11] Plasmon-enhanced tapered optical fibers, G. Blumberg, US Patent #7,054,528, issued May 30, 2006.

[12] Spectral Analysis with Evanescent Field Excitation, G. Blumberg and B.S. Dennis. US Patent #7,012,687, issued March 14, 2006.

[13] Spectral Analysis with Evanescent Field Excitation, G. Blumberg and B.S. Dennis. EP1593954, issued September 11, 2005.

[14] Plasmonic Device for Modulation and Amplification of Plasmonic Signals. G. Blumberg and B. Yurke. U.S. Patent application 20090195782, filed on August 6, 2009.

[15] Surface plasmon polariton modulation. G. Blumberg and V. Aksyuk. U.S. Patent application 20090122386, filed on May 14, 2009.

[16] Surface plasmon polariton modulation. V. Aksyuk and G. Blumberg. U.S. Patent #8,139,283, issued March 20, 2012.

[17] E. Ozbay, Plasmonics: Merging Photonics and Electronics at Nanoscale Dimensions, Science **311** 189 (2006).

[18] S. Lal, S. Link and N.J. Halas, Nature Photonics **1** 641 (2007).

[19] W.L. Barnes, A. Dereux and T.W Ebbesen, Suface plasmon subwavelength optics, Nature **424** 824 (2003).

[20] I.I. Smolyaninov, Y-J Hung, C.C. Davis, Magnifying superlens in the visible frequency range, Science **315** 1699 (2007).

[21] Surface-plasmon-assisted optical frequency conversion. G. Blumberg and Aref Chowdhury, U.S. Patent #8,005,331, issued August 23, 2011.

[22] S. I. Bozhevolnyi, V. S. Volkov, E. Devaux, J.-Y. Laluet, and T. W. Ebbesen, Channel plasmon subwavelength waveguide components including interferometers and ring resonators, Nature **440** 508 (2006).

[23] A. Hohenau, J. R. Krenn, A. L Stepanov, A. Drezet, H. Ditlbacher, B. Steinberger, A. Leitner and F.R. Aussenegg, Dielectric optical elements for surface plasmons, Optics Letters **30** 8 (2005).

[24] F. Aieta, P. Genevet, M.A. Kats, N. Yu, R. Blanchard, Z. Gaburro and F. Capasso, Aberration-Free Ultrathin Flat Lenses and Axicons at Telecom Wavelengths Based on Plasmonic Metasurfaces, Nano Lett. **12** 4932 (2012).

[25] S. T. Koev, A. Agrawal, H. J. Lezec, and V. A. Aksyuk, An efficient large-area grating coupler for surface plasmon polaritons, Plasmonics, published online November 2011, 1-9 (2011).

[26] Surface Plasmons Detector Based on a Field Effect Transistor. G. Blumberg. US Patent application 20090243589, filed October 1, 2009.

[27] T.W. Ebbesen, C. Genet and S.I. Bozhevolynyi, Surface-plasmon circuitry, Physics Today 61 44-50 (May 2008).

[28] J.A. Schuller, E.S. Barnard, W. Cai, Y.C Jun, J.S. White and M.L. Brongersma, Plasmonics for extreme light concentration and manipulation, Nature Materials 9, 193-204 (2010).

[29] M.I. Stockman, Nanoplasmonics: The physics behind the applications, Physics Today Feb. (2011).

[30] H. Ditlbacher, J.R. Krenn, N. Felidj, B. Lamprecht, G. Schider, M. Salerno, A. Leitner and F.R. Aussenegg, Fluorescence imaging of surface plasmon fields, Applied Physics Letters **80** 3 (2002).

[31] A. Hohenau, J. R. Krenn, A. Drezet, O. Mollet, S. Huant, C. Genet, B. Stein and T.W. Ebbesen, Surface plasmon leakage radiation microscopy at the diffraction limt, Optics Express **19** 25 (2011).

[32] M.I. Haftel, C. Schlockermann, and G. Blumberg, Applied Physics Letters 88, 193104 (2006).

[33] S. M. Orbons, A. Roberts, and D. N. Jamieson, M. I. Haftel, C. Schlockermann, D.Freeman and B. Luther-Davies, Applied Physics Letters 90, 251107 (2007).

[34] S. M. Orbons, M. I. Haftel, C. Schlockermann, D. Freeman, M. Milicevic, T. J. Davis, B. Luther-Davies, D. N. Jamieson, and A. Roberts, Optics Letters 33, 821 (2008).

[35] K. Yee, IEEE Trans. Ant. and Prop. 14, 302 (1966).

[36] J.-P. Berenger, J. Comp. Phys.,110, 185 (1994); S.D. Gedney, IEEE Trans. Ant. and Prop. 44, 1630 (1996). We use the latter version of PML.

[37] F. Lopez-Tejeira, F.J. Garcia-Vidal, and L. Martin-Moreno, Appl. Phys. A89, 251 (2007).

[38] F. Lopez-Tejeira, F.J. Garcia-Vidal, L. Martin-Moreno, Phys. Rev. B 72, 161 405(R) (2005).

[39] B. Lamprecht et al., Appl. Phys. Lett. 79, 51 (2001); P. Berini, Phys. Rev. B61, 10484 (2000); Phys. Rev. B63, 125417 (2001).